MASTER'S THESIS
DIPLOMARBEIT

FINITE ELEMENT ANALYSIS OF CONCRETE STRUCTURES SUBJECTED TO FIRE LOAD CONSIDERING DIFFERENT ELEMENT TYPES AND MATERIAL MODELS

FINITE ELEMENTE BERECHNUNG VON BETONTRAGWERKEN UNTER FEUERLAST UNTER BERÜCKSICHTIGUNG VERSCHIEDENER ELEMENTTYPEN UND MATERIALMODELLE

zum Zwecke der Erlangung des akademischen Grades eines
Diplom-Ingenieurs am

Institut für Mechanik der Werkstoffe und Strukturen - IMWS
der
TECHNISCHEN UNIVERSITÄT WIEN
unter der Anleitung von
Dipl.-Ing. **MATTHIAS ZEIML**
und
Univ.-Prof. Dipl.-Ing. Dr.techn. **ROMAN LACKNER**

durch

THOMAS RING

E 610 / 0325223
Am Berg 180
A-3921 Langschlag

Wien, im Juni 2008

Danksagung

Vorweg möchte ich mich bei all jenen bedanken, die zum Zustandekommen dieser Arbeit beigetragen haben.

In erster Linie widme ich meinen besonderen Dank meiner Familie, die mir das Studium ermöglicht und somit wesentlich zum erfolgreichen Abschluss dieser Arbeit beigetragen hat.

Für die sorgfältige Betreuung der Diplomarbeit möchte ich Herrn Dipl.-Ing. Matthias Zeiml meinen besonderen Dank aussprechen. Er hat mir sehr geholfen, neben dem fachlich vermittelten Wissen eine bessere Formulierung der vorliegenden englischsprachigen Diplomarbeit zu erreichen.
Danken möchte ich auch Herrn Univ.Prof. Dipl.-Ing. Dr.techn. Roman Lackner für die reibungslose Betreuung bei der Ausarbeitung meiner Diplomarbeit. Insbesonders möchte ich ihm für die fachliche Unterstützung bei der Lösungsfindung zu komplexen Fragestellungen danken.

Dank gebührt auch meinen Kollegen und Freunden im Bauingenieurwesen, die mir immer mit Rat und Tat zur Seite standen. Es sei an dieser Stelle auch all jenen gedankt, die mir hilfreich zur Seite standen und nicht namentlich erwähnt wurden.

Wien, im Juni 2008 Thomas Ring

Summary

Tunnel structures are an important part of public transport facilities. During recent years, large tunnel fires happened, having caused loss of human life and damage of tunnel support structures. Keeping this in mind, determination of the safety of these structures in case of fire loading is necessary in order to adopt the chosen design and, hence, to increase the safety in/of tunnels in case of fire.
The temperature distribution within support structures originating from fire loading is nonlinear with the highest temperature at the fire-exposed surface. Since this nonlinear temperature loading is difficult to be considered in numerical analysis tools, the nonlinear temperature distribution is converted into an equivalent (linear) temperature distribution. Most commercial design tools are able to take into account this equivalent temperature as input. Usually, the analysis is conducted assuming linear-elastic material behavior.

In this work, analyses are performed using both the equivalent and the nonlinear temperature distribution. Moreover, the effect of nonlinearities in the material behavior on the structural performance is investigated, considering linear-elastic and linear-elastic / ideal-plastic behavior. The analyses are performed with two finite element (FE) programs:

1. The FE program MARC: Hereby, user-defined subroutines developed at the Institute for Mechanics of Materials and Structures at Vienna University of Technology (TU Wien) are employed. This program allows consideration of nonlinearities as regards the material behavior and the temperature loading.

2. The FE program SOFISTIK: This program is restricted to linear temperature distributions and linear-elastic material behavior.

In this work, different structural systems are investigated (clamped beam, frame corner, and circular tunnel cross-section) and different boundary conditions are applied (either allowing or restraining longitudinal expansion / rotation).

The calculations considering linear-elastic material behavior and equivalent temperature distribution lead to almost identical results using SOFISTIK and MARC.
With SOFISTIK only linear-elastic analyses are performed, whereas also nonlinear analyses are performed with MARC. According to the obtained numerical values, consideration of linear-elastic / ideal-plastic material behavior in MARC leads to an increased compliance of the structure due to plasticity in areas loaded in tension of the investigated cross section and, thus, to reduced bending moments. This more realistic determination of the bending moment is important for the design of concrete and reinforced members.

Zusammenfassung

Die wichtige Rolle von Hohlraumbauten für den öffentlichen Infrastruktursektor wirft die Frage der Sicherheit solcher Strukturen im Brandfall auf. Nicht zuletzt aufgrund von Bränden in Tunnels in den letzten Jahren, die viele Todesopfer forderten und erheblichen Schaden an den Tragkonstruktionen verursachten, ist es wichtig das Tragverhalten einer Stuktur unter Feuerlast beurteilen zu können.
Die reale Temperaturverteilung innerhalb einer Struktur aufgrund einer Brandbelastung ist nichtlinear. Stand der Technik ist es, diese nichtlineare Temperatur in eine sogenannte äquivalente (lineare) Temperaturverteilung umzurechnen und damit die Bemessung durchzuführen. Vorteil dieser Vorgangsweise ist die mögliche Berücksichtigung der linearen Temperaturbelastung in vielen kommerziellen Bemessungsprogrammen. Neben der äquivalenten Temperaturverteilung wird die Bemessung unter Zugrundelegung von linear-elastischem Materialverhalten durchgeführt.

In dieser Arbeit werden Berechnungen unter Zugrundelegung sowohl der äquivalenten als auch der nichtlinearen Temperaturverteilung unter Berücksichtigung von linear-elastischem und linear-elastisch / ideal-plastischem Materialverhalten durchgeführt. Für die Berechnungen werden zwei Finite-Elemente (FE) Programme eingesetzt:

1. Das Finite-Elemente Programm MARC: In diesem Programm werden am Institut für Mechanik der Werkstoffe und Strukturen an der Technischen Universität Wien entwickelte "User-Subroutines" verwendet. Mit Hilfe dieses Programmes kann das nichtlineare Materialverhalten und die nichtlineare Temperaturverteilungen berücksichtigt werden.

2. Das Finite-Elemente Programm SOFISTIK: SOFISTIK erlaubt lediglich die Berücksichtigung der äquivalenten Temperaturverteilungen. Weiters wird ein linear-elastisches Materialverhalten zugrunde gelegt.

Im Weiteren werden in dieser Arbeit unterschiedliche statische Systeme untersucht (eingespannter Balken, eingespannte Rahmenecke und Tunnelquerschnitt). Diese statischen Systeme werden mit verschiedenen Randbedingungen berechnet (entweder freie oder behinderte Ausdehnung in Längsrichtung / Rotation).

Die Berechnung mit linear-elastischem Materialverhalten und äquivalenter Temperaturverteilung führt auf nahezu identische Ergebnisse mit den Programmen SOFISTIK und MARC. Mit Hilfe von SOFISTIK wird nur eine linear-elastische Schnittgrößenermittlung durchgeführt während auch nichtlineare Berechnungen mit MARC unter Berücksichtigung von linear-elastisch / ideal-plastischem Materialverhalten durchgeführt werden. Die erhaltenen Ergebnisse zeigen Plastizierung im Zugbereich des Querschnittes und eine vergrößerte Nachgiebigkeit des Tunnels. Die mit der Betonfestigkeit beschränkten Spannungen führen zu einer deutlichen Reduktion des

Biegemoments. Diese realitätsnahe Bestimmung der Momente ist für die Bemessung der Struktur unumgänglich.

Contents

1 Introduction

The structural analysis of tunnel structures should be able to consider nonlinear material behavior and complex loading situations. However, in engineering practice several simplifications are made regarding the applied loads and the employed material models. For the numerical analysis of tunnel structures, finite element (FE) programs are usually employed, assuming linear-elastic material behavior which leads to significant deviations from reality.
An important part of structural safety assessment is to consider the case of fire happening in the tunnel and to determine the response of the supporting structure to this accidental event (i.e., magnitude of damage / deformations of structure, occurrence of collapse). For this load case, the temperature distribution within the structure must be known and the relevant material characteristics must be taken into account. Several publications deal with the structural behavior of a tunnel under fire loading with different level of sophistication (see, e.g., [Richter and Hosser (2002); Wageneder (2002); El-Arabi et al. (1992); Schrefler et al. (2002); Pichler et al. (2006); Ahmed (2004)]).
The nonlinear temperature distribution present within the structure in case of fire loading can be considered in two ways:

1. The nonlinear temperature distribution is transferred into a so-called *equivalent temperature distribution*, characterized by a linear distribution over the cross section. It can be divided into two parts, a constant temperature increase T_m [°C] and a temperature gradient ΔT [°C/m]. Both T_m and ΔT can be considered within the beam theory.

2. The *nonlinear temperature* is directly implemented in the structural analysis. In this case, 3D or layered finite elements must be employed, enabling assignment of different temperatures within the structure.

This work presents results highlighting the advantages / disadvantages of consideration of (i) linear / nonlinear temperature distribution and (ii) different material models (linear-elastic and linear-elastic / ideal plastic).
The present work is divided into the following sections: In Section 2, the material models and considered structures are presented. The equivalent temperature concept is described in Section 3. Sections 4 to 5 contain the numerical results. A summarized interpretation of the results is given in Section 6.

2 Work scheme

2.1 Used programs

SOFISTIK[1] is a commercial FE program for the analyses of beams, slabs, 2D and 3D structures. The load case "fire" is considered by a linear temperature distribution (T_m and ΔT).

The FE-program MARC[2] is used together with user-subroutines, allowing consideration of elasto-plastic material behavior. In addition, layered finite elements are available (Figure 1). This allows specification of a nonlinear temperature distribution over the cross-section of the element.

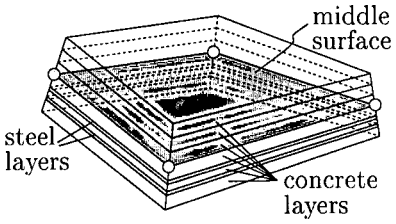

Figure 1: Illustration of layered finite shell elements as employed, e.g., in [Savov et al. (2003)]

2.2 Considered structural systems

The performance of SOFISTIK and MARC is compared by means of application to various structural problems (see Figure 2). For all structures, a strip of 1 m width is analyzed. In SOFISTIK, the structures are descretized by means of two-node beam elements (see Figure 2(d)), whereas four-node thick shell elements are employed within MARC (see Figure 2(e)).

[1] www.sofistik.de
[2] www.mscsoftware.com

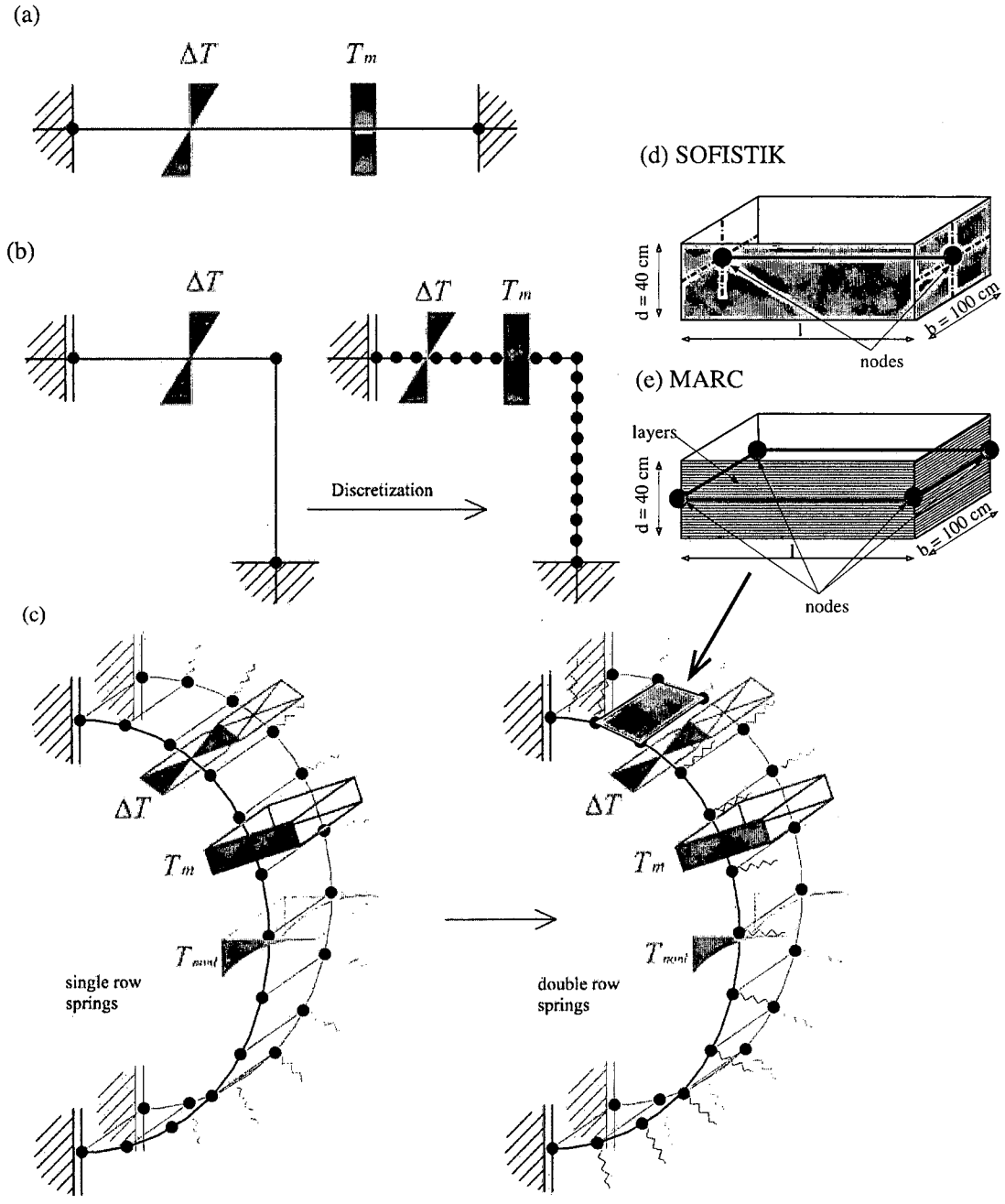

Figure 2: Considered structural systems: (a) clamped beam, (b) clamped frame corner, and (c) tunnel cross-section; Finite elements used in analyses: (d) beam element (SOFISTIK) and (e) shell element (MARC)

2.3 Material behavior

The calculations are performed using

1. linear-elastic and
2. linear-elastic / ideal-plastic

material models. The stress-strain curves of the considered material models are given in Figure 3. For the presented analyses, the material parameters describing the elasto-plastic behavior of concrete are set to:

- Young's modulus: $E_c = 30.000$ MPa
- Uniaxial compressive strength: $f_c = 30$ MPa
- Poisson's ratio: $\nu = 0.2$
- Strain at compressive strength: $\varepsilon_{ci} = 0.0022$

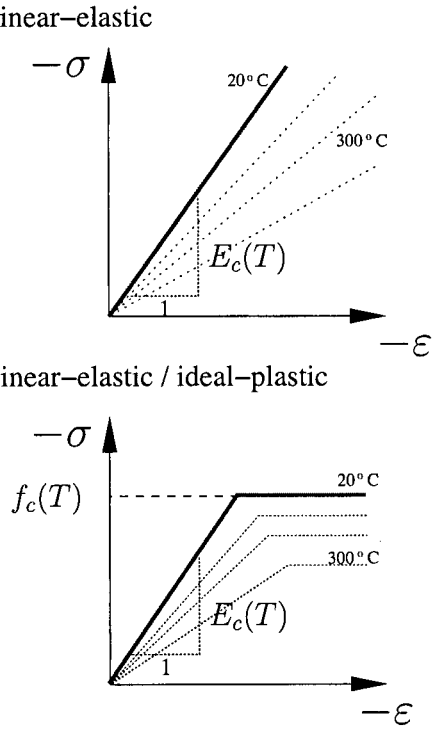

Figure 3: Considered material models

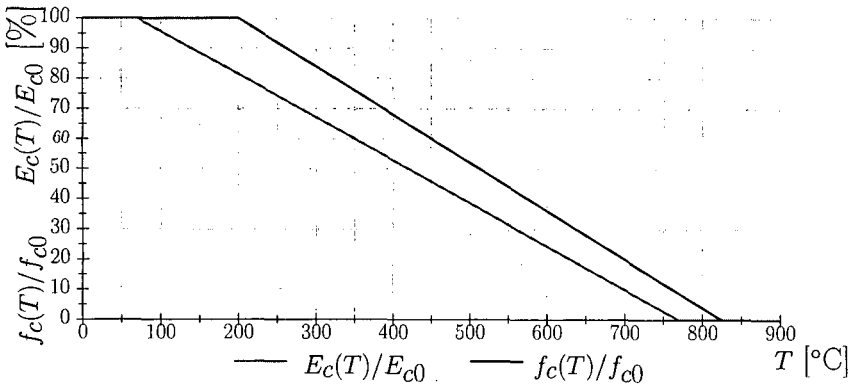

Figure 4: Temperature-dependent reduction of compressive strength $f_c(T)$ and Young's modulus $E_c(T)$ [prEN1992–1–2 (2004); Kusterle et al. (2004)]

The temperature-dependent degradation of the material parameters of concrete (see Figure 4) is taken from national and international standards [prEN1992–1–2 (2004); Kusterle et al. (2004)].

2.4 Load cases

Within the tunnel analysis, different load cases are considered:

- Dead load – G:
  The tunnel lining has a thickness of 0.4 m (see Figure 5). The shotcrete lining is not considered in this load case. The considered inner concrete tunnel lining has a specific weight of $\gamma_c = 25$ kN/m^3.

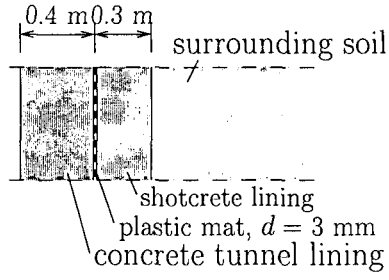

Figure 5: Tunnel structure

- Earth load – E:
  The pressure of the surrounding soil is converted into nodal forces. The material parameters of the earth layers are shown in Figure 6. Since the same FE discretization is used for both FE programs, the nodal forces representing the earth load are the same.

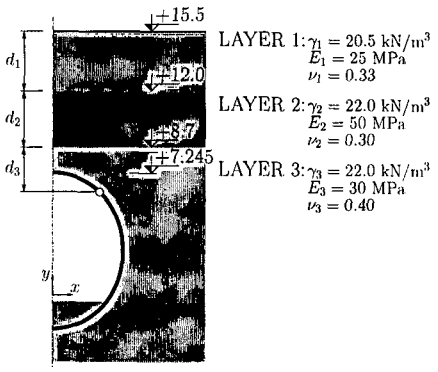

Figure 6: Soil layers

- Equivalent temperature loading:
  The nonlinear temperature distribution is transferred into a linear distribution, with T_m and ΔT, in order to serve as input for the beam model. The determination of T_m and ΔT is explained in Subsection 3.2.

- Nonlinear temperature loading:
  The nonlinear temperature distribution is obtained by solving the 1D energy-balance equation. (See Section 3).

In the following, the five load cases are referenced with the symbols presented in Figure 7.

Figure 7: Symbols for considered load cases

2.5 Output parameters used for comparison

For determination of the influence of the different model specifications (material behavior, temperature loading, etc.) on the structural response, the following results are compared:

- Normal force N [kN]
- Bending moment M [kNm]
- Top displacement v_{top} [m] (in case of tunnel analysis)

3 Temperature load

3.1 General

When a structure is subjected to fire, heat is transferred from the fire source towards the surface of the structure and subsequently further into the concrete. Hence, the temperature rises within the structure, influencing strength and stiffness of concrete and, therefore, the compliance of the whole structure.
The first step towards determination of the structural response of a tunnel under fire load is the definition of the fire load itself, depending on the burning goods (i.e., car tires, wood, fuel etc.). The burning good influences the speed of the temperature increase and the maximum temperature. Typically, tunnel fires are characterized by a quick temperature increase in the first minutes of the fire up to approx. 1200°C. The temperature history used within this thesis is shown in Figure 8. After 90 min, the fire temperature decreases, assuming fire fighting measures taking place. The thick continuous line shows the surface temperature used in the analysis, which was determined from large-scale fire experiments. The temperature distribution within the structure is obtained by means of a coupled FE-analysis, solving the energy and mass-transport problem in a coupled manner (see Figure 9). Detailed information on the calculation of the temperature distribution within the structure can be found in [Zeiml (2004); Zeiml et al. (2007)].

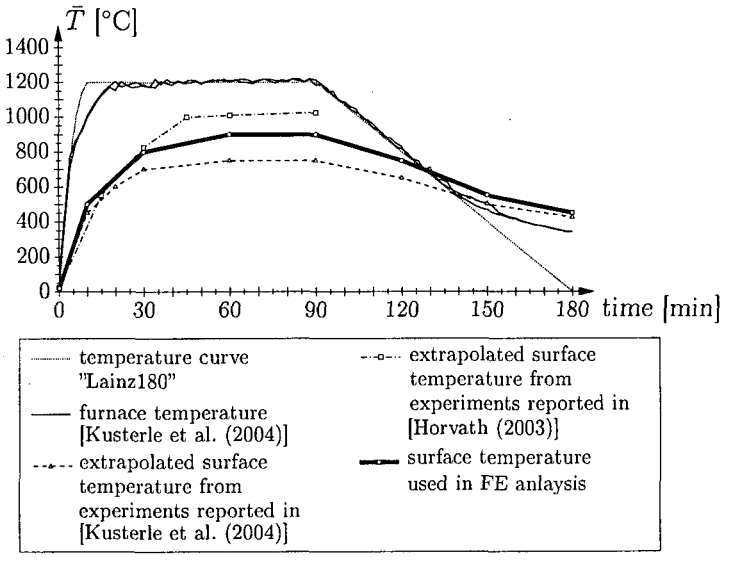

Figure 8: Temperature history used within analyses (surface temperature)

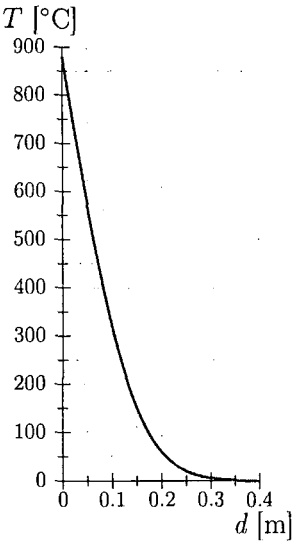

Figure 9: Nonlinear temperature distribution at $t = 2.0$ h (thickness of lining: 40 cm)

3.2 Equivalent temperature distribution

Fire loading of a concrete structure results in nonlinear temperature distribution over the cross-section (see Figure 9). For calculations using beam elements, the nonlinear temperature distribution is transferred into an equivalent (linear) temperature distribution, consisting of:

- constant temperature increase: T_m [°C]
- temperature gradient: ΔT [°C/m]

Figure 10 shows both the nonlinear temperature distribution and corresponding equivalent temperature distribution. In addition to the use of an equivalent temperature distribution, the temperature-dependent Young's modulus of the cross-section is averaged over the cross-section using the nonlinear temperature distribution, serving as input for the beam elements.

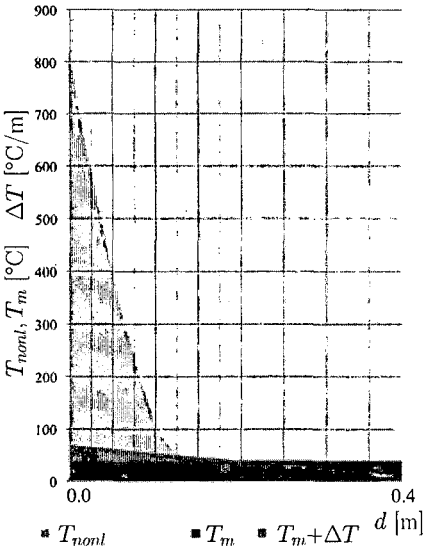

Figure 10: Nonlinear / linear temperature distribution at $t = 1.5$ h (thickness of lining: 40 cm)

T_m and ΔT are determined according to [Wageneder (2002); Kusterle and Lindlbauer (2004)]. Hereby, the cross-section is divided into several layers. Using the nonlinear temperature distribution, the following parameters can be determined for each layer (see Figure 11):

- Compressive strength: $f_{c,i}(T_i)$ [MPa]
- Young's modulus: $E_{c,i}(T_i)$ [MPa]
- Thermal expansion: $\varepsilon_i^{th}(T_i)$ [–]
- Stress: $\sigma_i(T_i)$ [MPa]

Hereby, the thermal expansion of the i-th layer is given by

$$\varepsilon_i^{th}(T_i) = \alpha(T_i - T_0), \tag{1}$$

giving the respective stress within the i-th layer by[3]

$$\sigma_i(T_i) = E_c(T_i)\varepsilon_i^{th}(T_i) \leq f_c(T_i)\,. \tag{2}$$

[3] $f_{c,i}$ is the uniaxial compressive strength. In order to consider the confining stress in the longitudinal direction, the biaxial compressive strength $f_{b,i}$, with $f_{b,i} = 1.16 f_{c,i}$, may be used.

In Equations (1) and (2), α [°C^{-1}] is the thermal dilation coefficient of concrete given by $1.0{\cdot}10^{-5}$, T_i [°C] is the temperature of the i-th layer, and T_0 [°C] is the initial temperature. By summation of $\sigma_i(T_i)$ over all layers, the normal force and the bending moment are obtained by

$$N_{equ} = \sum_{i=1}^{N} \sigma_i(T_i) A_i \tag{3}$$

and

$$M_{equ} = \sum_{i=1}^{N} \sigma_i(T_i) A_i e_i \,, \tag{4}$$

where N is the number of layers, A_i the cross-sectional area of the i-th layer, and e_i [m] the distance of the i-th layer to the middle plane of the cross-section.
N_{equ} and M_{equ} are used to determine T_m and ΔT as

$$T_m = \frac{N_{equ}}{E_{equ} \alpha A} \tag{5}$$

and

$$\Delta T = \frac{M_{equ}}{E_{equ} \alpha I} \,, \tag{6}$$

where A [m^2] and I [m^4] are the cross-sectional area and the moment of inertia, respectively. E_{equ} [MPa] is the equivalent Young's modulus, given by

$$E_{equ} = \sum_{i=1}^{N} \frac{E_{c,i}(T_i) A_i}{A} \,. \tag{7}$$

The parameters T_m, ΔT, and E_{equ} serve as input for the analysis using beam elements. Figure 11 illustrates the outlined procedure. In fact, the equivalent temperature distribution considering linear-elastic material behavior gives the same internal stress resultants as the nonlinear temperature distribution for the special case of a clamped beam (see also Appendix B).

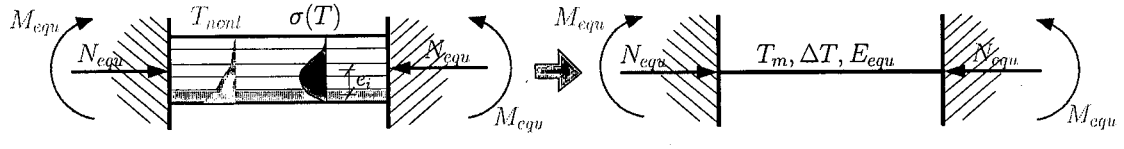

Figure 11: Structural model and loading for determination of T_m and ΔT

Figure 12 shows the temperature and stress distribution within the clamped beam for selected time instants. The maximum value of the stress distribution moves towards the middle plane of the cross-section as the heat progresses further into the structure with the duration of fire loading.

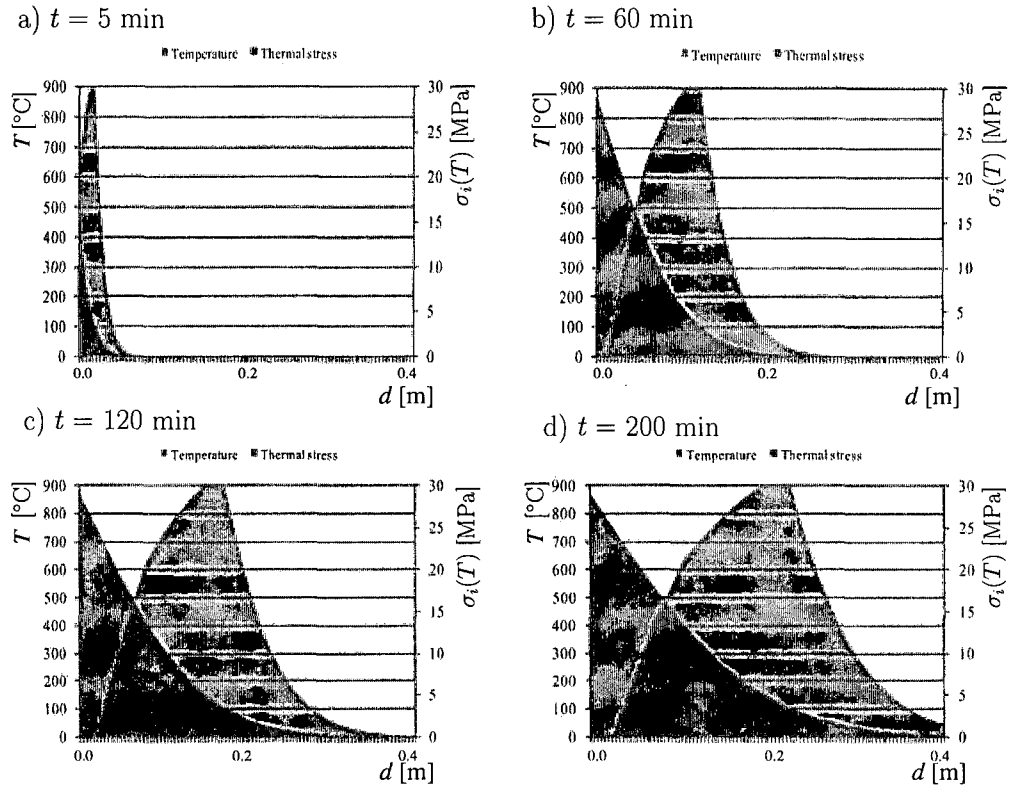

Figure 12: Stress distribution for selected time instants of fire loading

Based on the temperature and stress distribution, the evolution of T_m, ΔT, and E_{equ} is computed (see Figure 13). Hereby, the following is observed:

1. E_{equ}:
   The equivalent Young's modulus is decreasing with increasing duration of fire loading since heat moves into the cross-section, damaging the material.

2. T_m:
   Since the temperature in the cross-section is increasing, the constant temperature T_m is also increasing.

3. ΔT:
   Caused by the increasing thermal load, ΔT increases up to $t \approx 1.1$ hours and is decreasing afterwards. This behavior is explained by the stress distribution (Figure 12), moving towards the middle plane of the cross-section with increasing time.

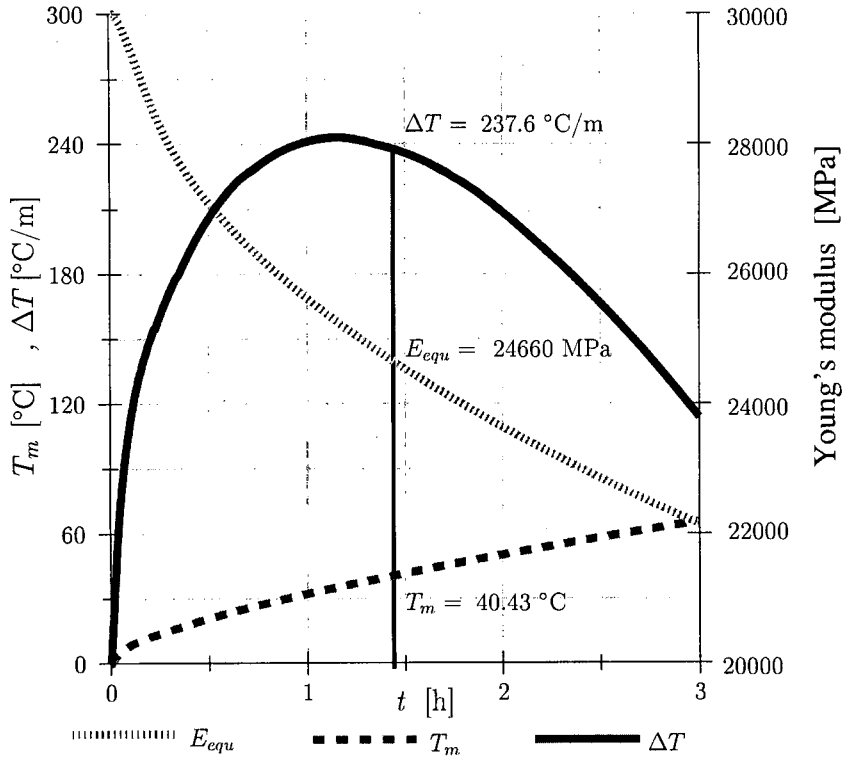

Figure 13: Equivalent temperature parameters determined from Equations (5) to (7) considering temperature loading depicted in Figure 8 (thickness of lining: 40 cm)

For reasons of comparison, three time instants, with $t = 1.0$, 1.43, and 2.4 h, were selected. Table 1 contains the respective quantities for E_{equ}, T_m, and ΔT.

t [h]	E_{equ} [MPa]	T_m [°C]	ΔT [°C/m]
1.00	25604	32.28	241.1
1.43	24660	40.43	237.6
2.40	22987	56.64	174.8

Table 1: Equivalent temperature parameters for $t = 1.0$, 1.43, and 2.4 h

3.3 Nonlinear temperature distribution

In case layered shell elements are used within the structural analysis, the equivalent temperature distribution is not necessary and the more realistic nonlinear temperature distribution can be used. The temperature distributions are obtained by solving the coupled energy and mass-transport problem [Zeiml et al. (2007)] (see Figure 14 for temperature distribution for selected time instants).

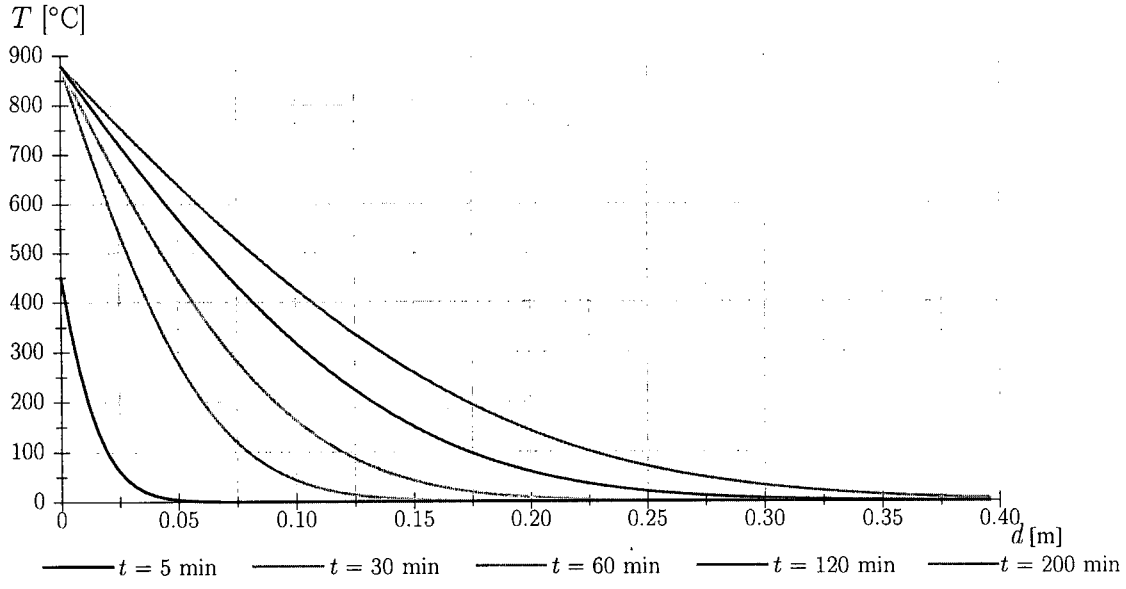

Figure 14: Nonlinear temperature distribution for selected time instants [Zeiml et al. (2007)] (thickness of lining: 40 cm)

4 Results – linear-elastic material behavior

4.1 Clamped beam – equivalent temperature distribution (LC T_m, ΔT)

Figure 15 shows the considered structural model, discretizied by a single finite element of thickness 0.4 m fixed against longitudinal displacement in X-direction and rotation in Z-direction at both ends. This yields a statically undetermined system, with T_m inducing a restrained normal force and ΔT inducing a restrained bending moment.

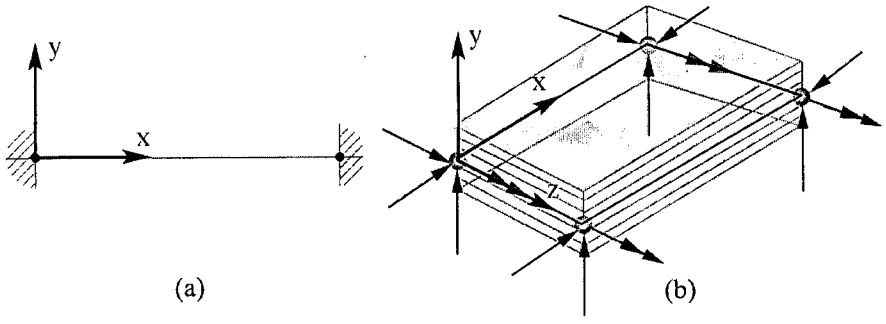

Figure 15: Clamped beam: FE model used in (a) SOFISTIK and (b) MARC

In this example, a linear temperature distribution is considered, with T_m and ΔT according to Figure 13. Dead load is neglected.

Figure 16 shows the distribution of the thermally-induced stresses over the beam element

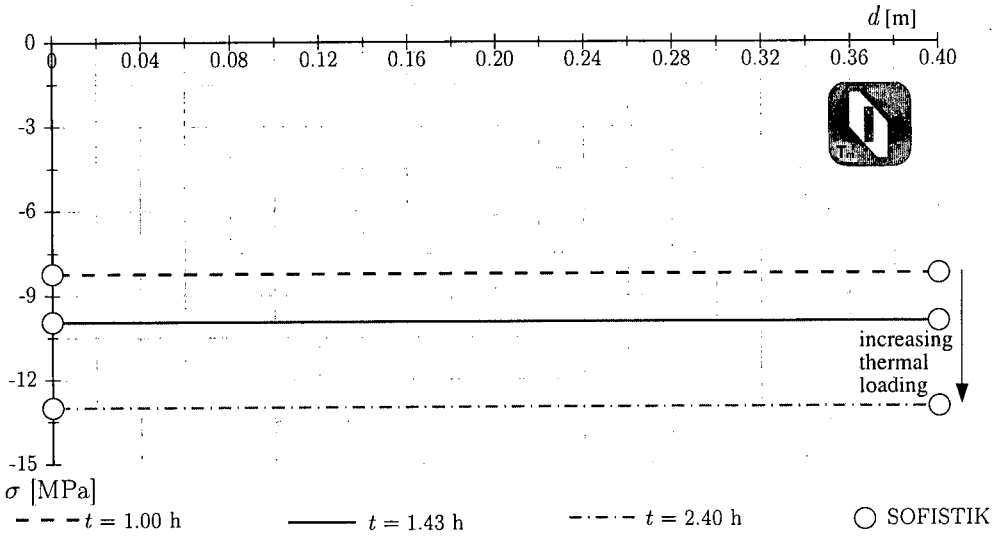

Figure 16: Results – stress distribution for selected time instants (LC T_m)

in consequence of T_m for three selected time instants. Figure 17 shows the thermally-induced normal forces, giving the same results for SOFISTIK and MARC.

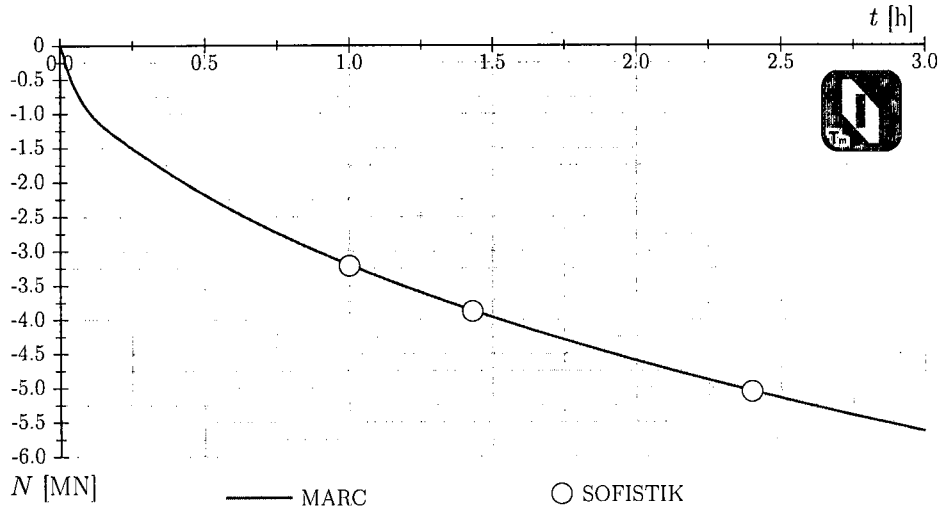

Figure 17: Results – normal force as a function of time (LC T_m)

Figure 18 shows the thermally-induced stresses in consequence of LC ΔT for three selected time instants, showing a linear distribution over the element thickness. The maximum stress is reached at $t \approx 1.0$ h, corresponding to the evolution of ΔT in Figure 13.

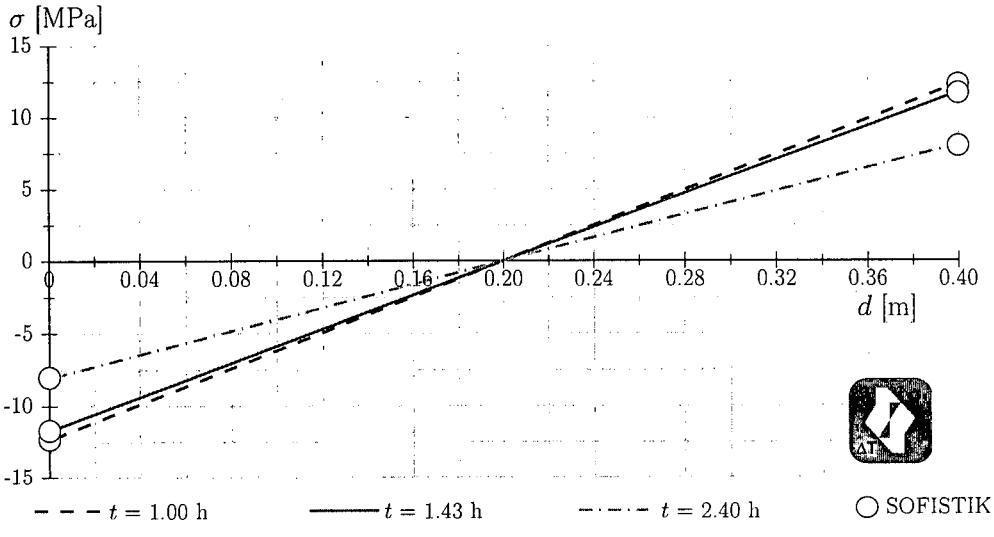

Figure 18: Results – stress distribution for selected time instants (LC ΔT)

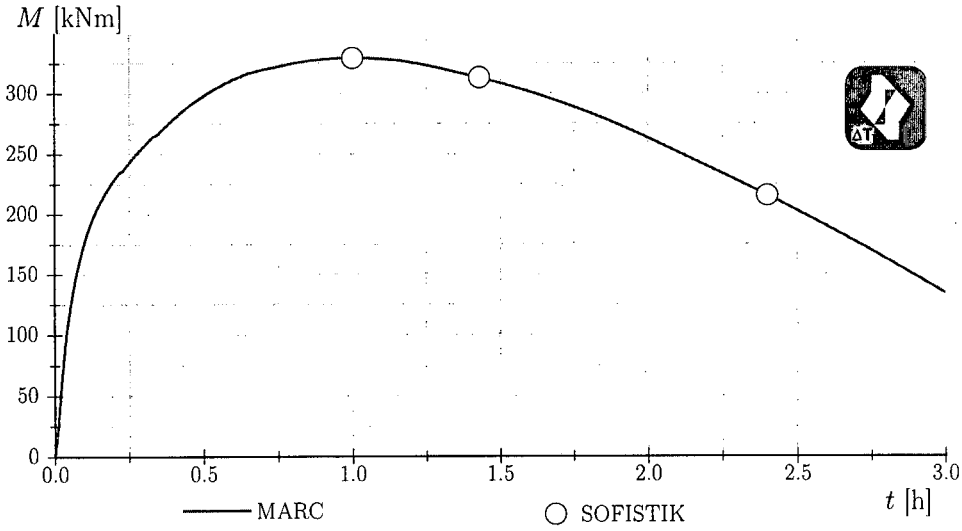

Figure 19: Results – bending moment as a function of time (LC ΔT)

The respective bending moment in consequence of ΔT is given in Figure 19. So far, both FE programs (SOFISTIK, MARC) give similar results (see Figures 17 and 19).

4.2 Clamped frame corner – equivalent temperature distribution (LC T_m, ΔT)

Two finite elements are connected at an angle of 90° to form the frame corner. The boundary conditions are given in Figure 20. The frame is clamped at both ends except for the upper end, where the displacement in Y-direction is not restrained. In this simu-

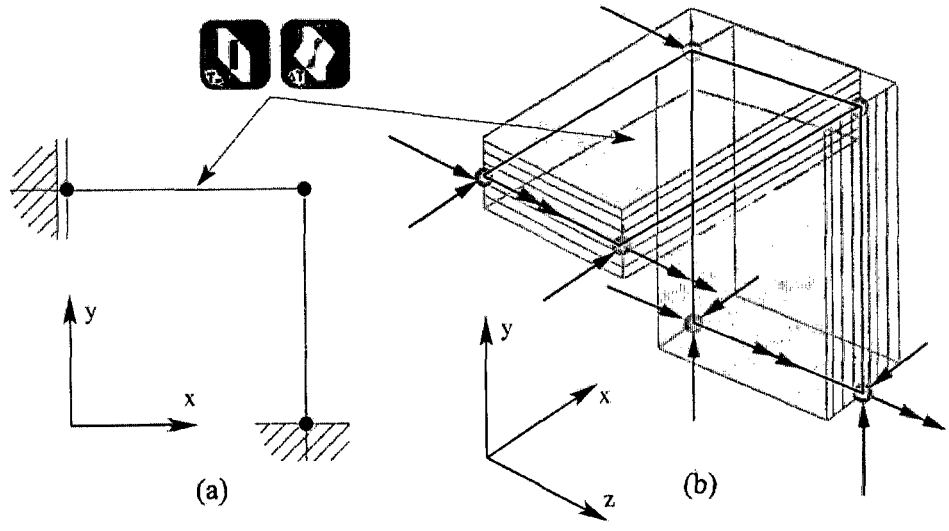

Figure 20: Clamped corner frame: FE model used in (a) SOFISTIK and (b) MARC

lation, only the upper (horizontal) part of the frame is loaded by the equivalent (linear) temperature distribution, given by $T_m(t)$ and $\Delta T(t)$ according to Figure 13.

For the system shown in Figure 20 and the considered type of loading, the FE discretization influences the numerical results. Accordingly, three FE meshes were considered in the FE analyses using MARC as shown in Figure 21. SOFISTIK, on the other hand, subdivides each part of the frame into a sufficient number of finite elements.

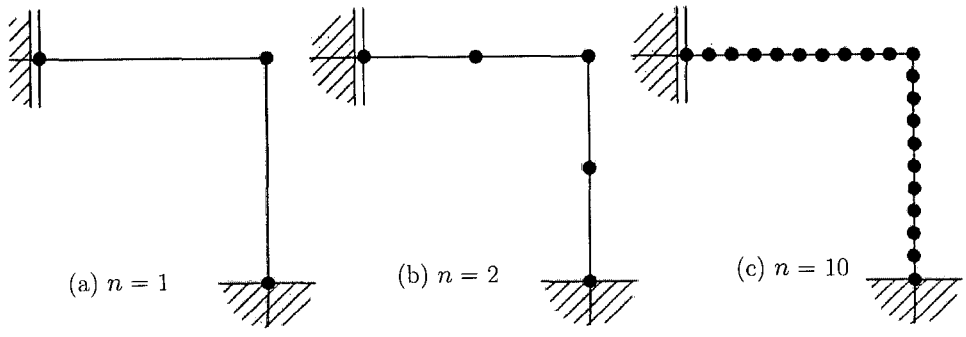

Figure 21: FE mesh refinement steps performed within analyses using MARC (case with $n = 1$ is sufficient for SOFISTIK)

Figure 22 shows the stresses related to the compressive strength at $t = 1.43$ h obtained with SOFISTIK for the LC T_m. From these results, the internal stress resultants (i.e., normal force and bending moment) are calculated (see Figure 23).

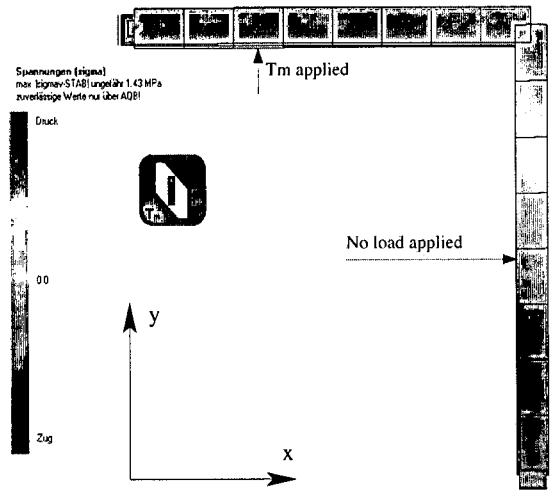

Figure 22: Results SOFISTIK – stress distribution for $t = 1.43$ h (LC T_m)

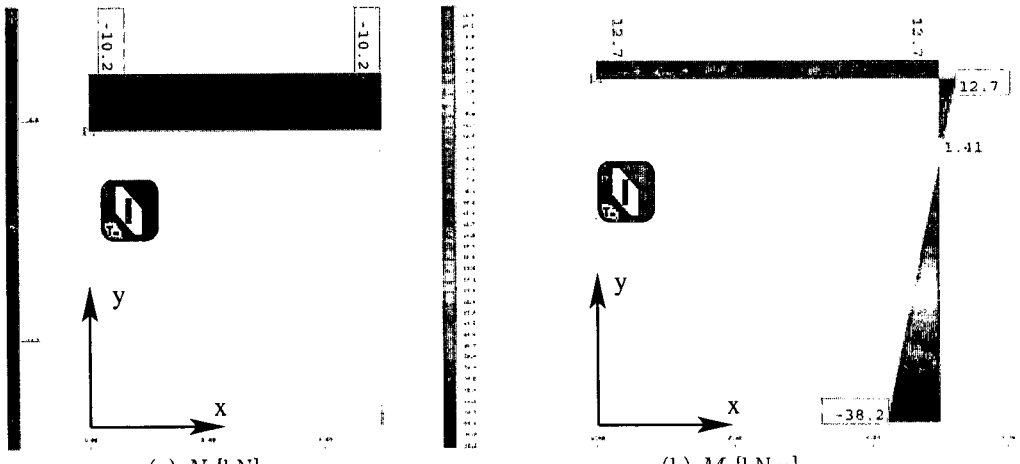

(a) N [kN] (b) M [kNm]

Figure 23: Results SOFISTIK – (a) normal force and (b) bending moment at $t = 1.43$ h (LC T_m)

Tables 2, 3, and 4 contain the normal force and bending moment obtained from MARC for this LC and the three FE meshes shown in Figure 21. The results depend on the underlying FE mesh, approaching the results obtained from SOFISTIK with increasing number of elements n.
Within MARC, 4-node layered shell elements are used with four integration points per element (see Figure 24). In general, the elements closer to the corner show a larger

variation of internal forces within the element (the respective values obtained at the four integration points are given in the tables in parentheses). Taking the average value from the respective four integration points levels out that variation.

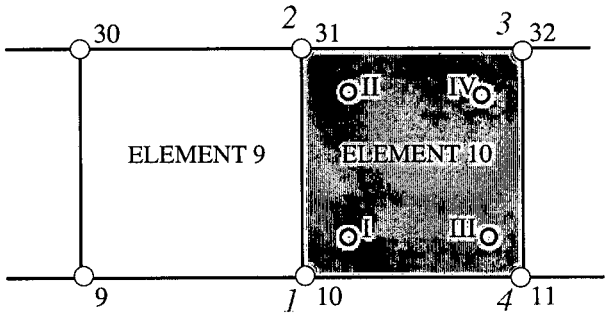

...9,10,11,12... Global node numbers *1,2,3,4* Local node numbers I,II,III,IV Integration points

Figure 24: Integration points for MARC shell element

	Element	Normal force N [kN]	Bending moment M [kNm]
Upper beam	1	-17.3 (126.7/194.1/-228.6/-161.2)	21.5 (21.3/21.5/21.6/21.8)
Lower beam	2	0.0 (211.7/143.7/-143.7/-211.7)	-21.5 (-21.6/-21.8/-21.3/-21.5)

Table 2: Results MARC ($n = 1$) – normal force and bending moment at $t =$ 1.43 h (values in parentheses are results at integration points) (LC T_m)

	Element	Normal force N [kN]	Bending moment M [kNm]
Upper	1	-11.4 (-51.9/-57.6/34.8/29.0)	14.3 (14.4/14.3/14.3/14.2)
beam	2	-11.4 (29.8/247.8/-270.6/-52.6)	14.3 (14.0/14.2/14.4/14.6)
Lower	3	0.0 (262.3/38.5/-38.5/-262.3)	0.0 (-0.6/-0.08/0.1/0.7)
beam	4	0.0 (-47.2/-39.9/39.9/47.2)	-28.6 (-28.4/-29.1/-28.0/-28.7)

Table 3: Results MARC ($n = 2$) – normal force and bending moment at $t =$ 1.43 h (values in parentheses are results at integration points) (LC T_m)

	Element	Normal force N [kN]	Bending moment M [kNm]
	1	-10.2	12.75
	2	-10.2	12.75
	3	-10.2 (-9.8/-10.6/-9.8/-10.6)	12.75
	4	-10.2 (-9.1/-11.3/-9.1/-11.3)	12.75
Upper	5	-10.2 (-9.2/-11.7/-8.7/-11.2)	12.75
beam	6	-10.2 (-16.5/-6.0/-14.4/-3.9)	12.75
	7	-10.2 (-52.9/27.5/-47.9/32.5)	12.75
	8	-10.2 (-165.5/148.1/-161.3/145.1)	12.75
	9	-10.2 (-350.3/364.8/-385.2/320.0)	12.7 (12.9/12.6/12.9/12.6)
	10	-10.2 (-134.6/330.0/-50.3/114.2)	12.7 (11.8/13.2/12.3/13.7)
	11	0.0 (355.0/-137.4/137.4/-355.0)	10.2 (9.0/10.9/9.5/ 11.4)
	12	0.0 (381.8/-346.9/346.9/-381.8)	5.1 (5.0/5.1/5.1/5.2)
	13	0.0 (153.0/-157.5/157.5/-153.0)	0.0
	14	0.0 (37.9/-43.1/43.1/-37.9)	-5.1 (-5.2/-5.2/-5.0/-5.0)
Lower	15	0.0 (4.2/-6.3/6.3/-4.2)	-10.2 (-10.3/-10.3/-10.1/-10.1)
beam	16	0.0	-15.3 (-15.4/-15.4/-15.2/-15.2)
	17	0.0	-20.4 (-20.4/-20.5/-20.3/-20.3)
	18	0.0	-25.5 (-25.6/-25.5/-25.4/-25.4)
	19	0.0	-30.6 (-30.7/-30.6/-30.6/-30.5)
	20	0.0	-35.7 (-34.1/-37.4/-34.0/-37.3)

Table 4: Results MARC ($n = 10$) – normal force and bending moment at $t =$ 1.43 h (values in parentheses are results at integration points) (LC T_m)

Figure 25 shows the stresses obtained from SOFISTIK for LC ΔT applied at the upper (horizontal) part of the frame, resulting in both bending moment and normal force. The results obtained from MARC are given in Tables 5 to 7, converging for increasing number of elements to the results obtained from SOFISTIK.

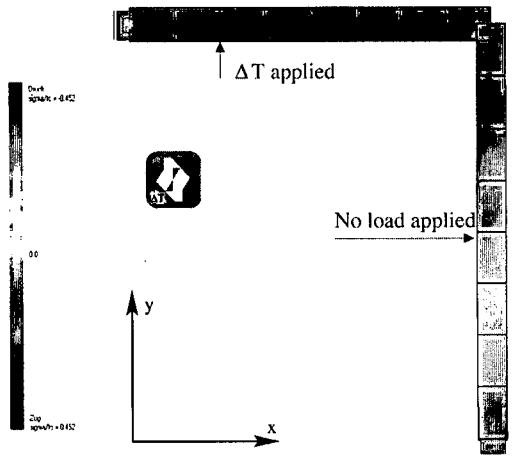

Figure 25: Results SOFISTIK – stress distribution at $t = 1.43$ h (LC ΔT)

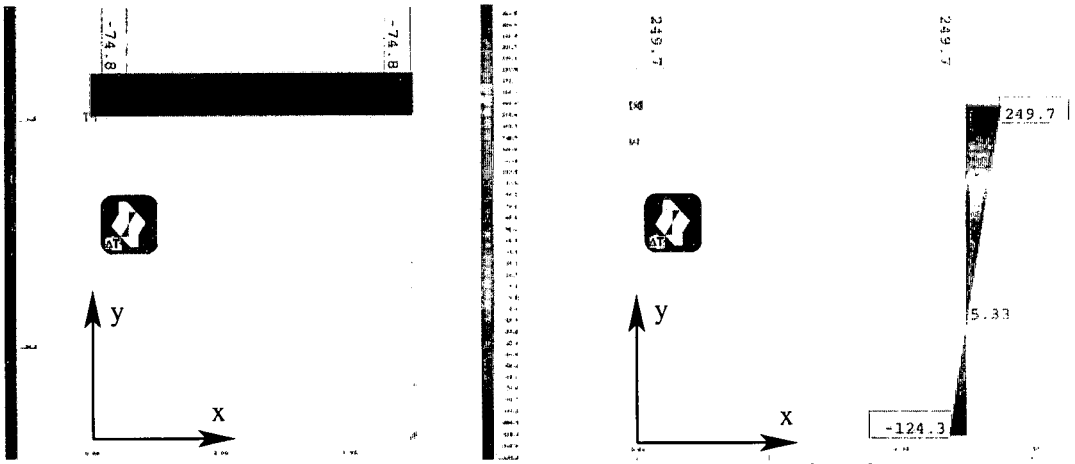

a) N [kN] b) M [kNm]

Figure 26: Results SOFISTIK – (a) normal force and (b) bending moment at $t = 1.43$ h (LC ΔT)

	Element	Normal force N [kN]	Bending moment M [kNm]
Upper beam	1	-125.1 (-123.7/-123.1/-127.1/-126.5)	315.1 (307.5/307.5/322.6/322.6)
Lower beam	2	0.0 (0.2/0.1/-0.1/-0.2)	226.5 (227.7/227.5/226.1/225.9)

Table 5: Results MARC ($n = 1$) – normal force and bending moment at $t = 1.43$ h (values in parentheses are results at integration points) (LC ΔT)

	Element	Normal force N [kN]	Bending moment M [kNm]
Upper	1	-83.7 (-84.2/-84.4/-82.9/-83.1)	262.4 (264.2/264.2/260.5/260.5)
beam	2	-83.6 (-83.2/-80.3/-86.9/-84.0)	262.4 (256.2/256.2/268.5/268.5)
Lower	3	0.0 (-3.2/0.6/-0.6/3.2)	157.8 (156.7/156.7/158.9/158.9)
beam	4	0.0	-51.3 (-53.3/-53.3/-49.2/-49.2)

Table 6: Results MARC ($n = 2$) – normal force and bending moment at $t =$ 1.43 h (values in parentheses are results at integration points) (LC ΔT)

	Element	Normal force N [kN]	Bending moment M [kNm]
	1	-74.9	250.4
	2	-74.9	250.4
	3	-74.9	250.4
	4	-74.9	250.4
Upper	5	-74.9	250.4
beam	6	-74.9 (-75.0/-74.9/-75.0/-74.8)	250.4
	7	-74.9 (-75.7/-74.2/-75.6/-74.1)	250.4
	8	-74.9 (-77.7/-72.2/-77.7/-72.1)	250.4
	9	-74.9 (-82.9/-66.7/-83.1/-66.9)	250.4 (250.5/250.5/250.3/250.3)
	10	-74.9 (-78.3/-66.6/-83.2/-71.5)	250.4 (246.9/246.9/253.9/253.9)
	11	0.0 (-14.7/8.2/-8.2/14.7)	231.6 (231.8/231.8/231.4/231.4)
	12	0.0 (-8.4/11.9/-11.9/8.4)	194.1 (193.7/193.7/194.6/194.6)
	13	0.0 (0.9/-1.1/1.1/-0.9)	156.7 (156.3/156.3/157.2/157.2)
	14	0.0	119.3 (118.8/118.8/119.7/119.7)
Lower	15	0.0	81.9 (81.4/81.4/82.3/82.3)
beam	16	0.0	44.4 (43.9/43.9/44.8/44.8)
	17	0.0	6.9 (6.5/6.5/7.4/7.4)
	18	0.0	-30.5 (-30.9/-30.9/-30.1/-30.1)
	19	0.0	-67.9 (-68.4/-68.4/-67.5/-67.5)
	20	0.0	-105.4 (-105.6/-105.7/-105.2/-105.2)

Table 7: Results MARC ($n = 10$) – normal force and bending moment at $t =$ 1.43 h (values in parentheses are results at integration points) (LC ΔT)

Figure 27 illustrates the effect of the discretization on the normal force and bending moment for LC ΔT, showing almost equal values for the SOFISTIK-results and the MARC-results using the FE mesh with $n = 10$.

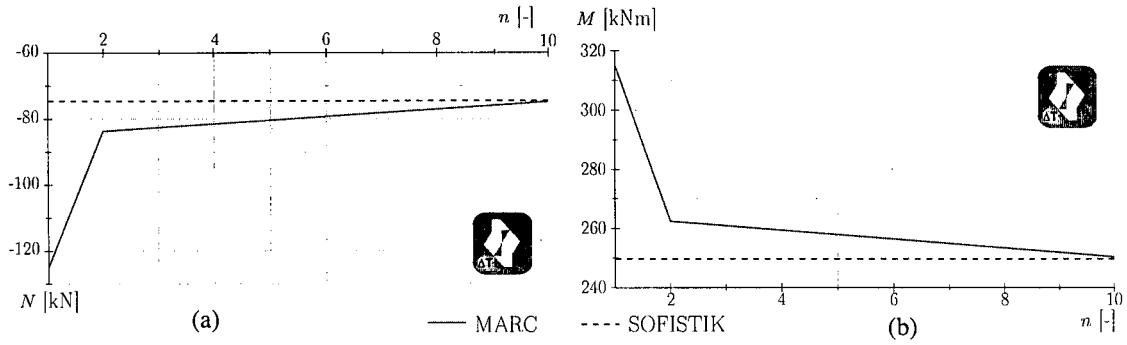

Figure 27: (a) Normal force N and (b) bending moment M in upper beam as a function of used elements n (LC ΔT)

Figure 28 shows the normal force obtained from MARC at the integration points (see also Table 3). The specification of the integration points is shown in Figure 24.

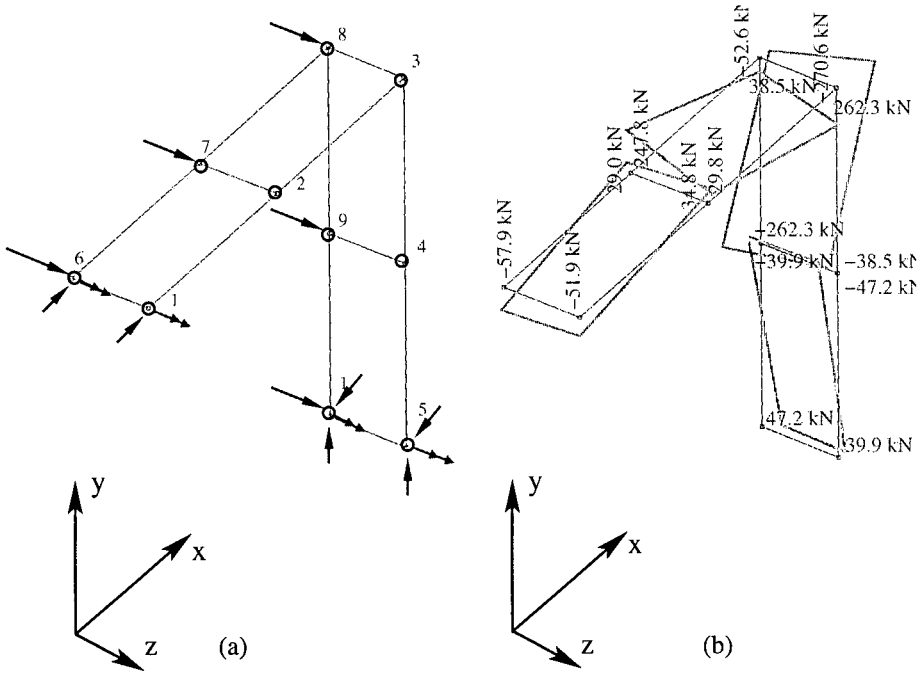

Figure 28: Results MARC – (a) boundary conditions and (b) normal force at integration points for FE mesh with $n = 2$ (LC T_m)

The average value over the four integration points, however, results in values comparable to the SOFISTIK-results.

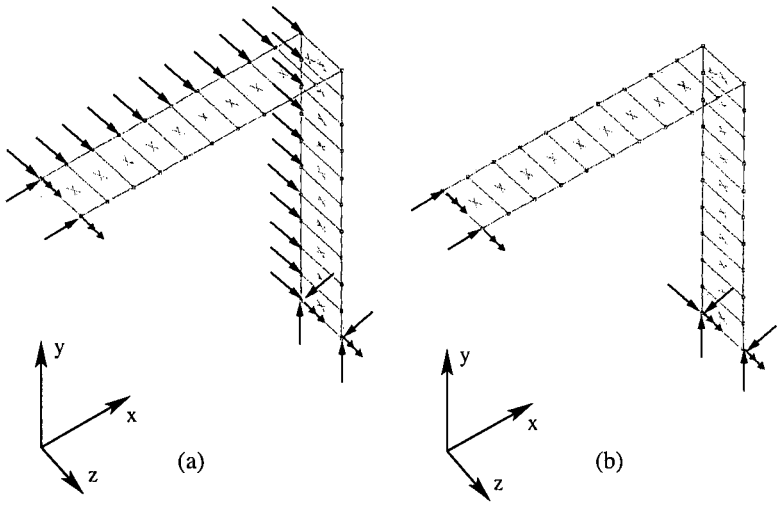

Figure 29: Different boundary conditions in Z-direction: (a) fixed-displacement at one side of the frame; (b) fixed-displacement only at one node (bottom support) – $n = 10$ (LC T_m)

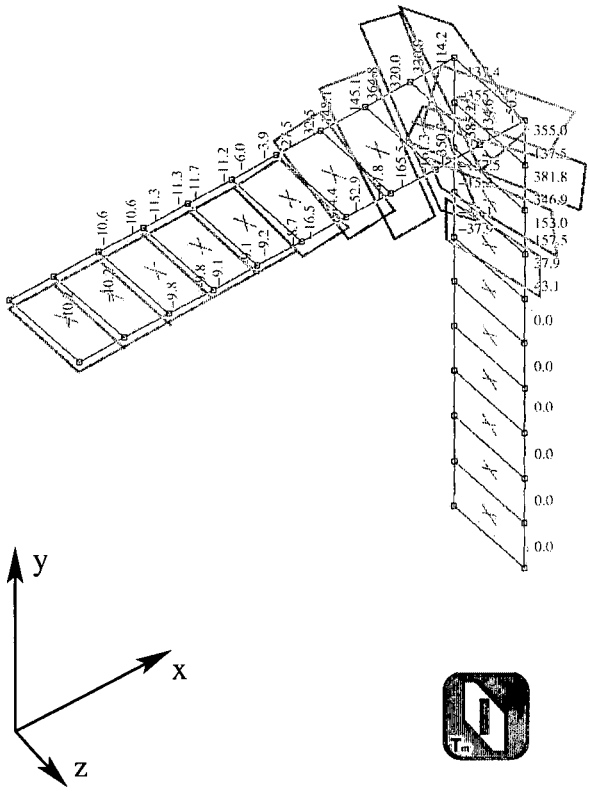

Figure 30: Results MARC ($n = 10$) – normal force at integration points considering boundary conditions depicted in Fig. 29(a) (LC T_m)

Figures 30 and 31 illustrate the influence of two different types of boundary conditions in Z-direction (see Figure 29) on the normal force distribution. Fixing one side of the frame in Z-direction results in large variation of the results at the integration points close to the frame corner along the Z-direction. Near the supports, this variation vanishes. When the system is fixed in Z-direction only at one node (bottom support in Figure 31), the variation of the normal force in Z-direction vanishes.

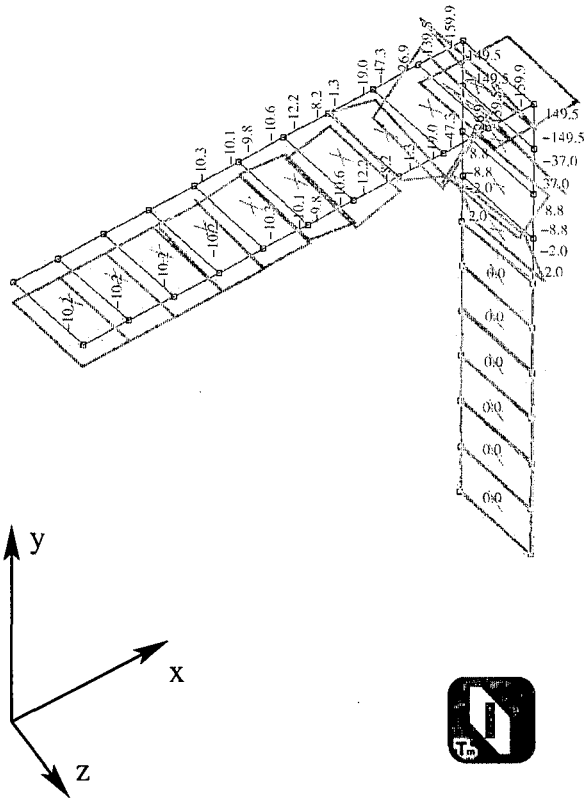

Figure 31: Results MARC ($n = 10$) – normal force at integration points considering boundary conditions depicted in Figure 29(b) (LC T_m)

Summing up, the difference between the results from SOFISTIK and MARC in case a sufficiently fine discretization is small, amounting 0.7 kNm (0.28%) for the bending moment using the FE mesh with $n = 10$.

4.3 Tunnel cross-section – equivalent temperature distribution (All LC)

Exploiting symmetry, only one half of the tunnel cross-section is analyzed. The surrounding soil is modeled by means of spring elements, acting only in compression. The stiffness of each spring is calculated by [Savov et al. (2003)]

$$K = \frac{E}{1+\nu}\frac{A}{R}, \tag{8}$$

where E [MPa] is Young's modulus, ν [–] is Poisson's ratio of the surrounding soil, and A [m^2] is the specific sub area related to the respective FE-node. Radius R [m] is set equal to the average of radii $R_1 = 3.85$ m and $R_2 = 5.55$ m of the considered cross-section (see Figure 32). As illustrated in Figure 32, the FE-model of SOFISTIK consists of beam

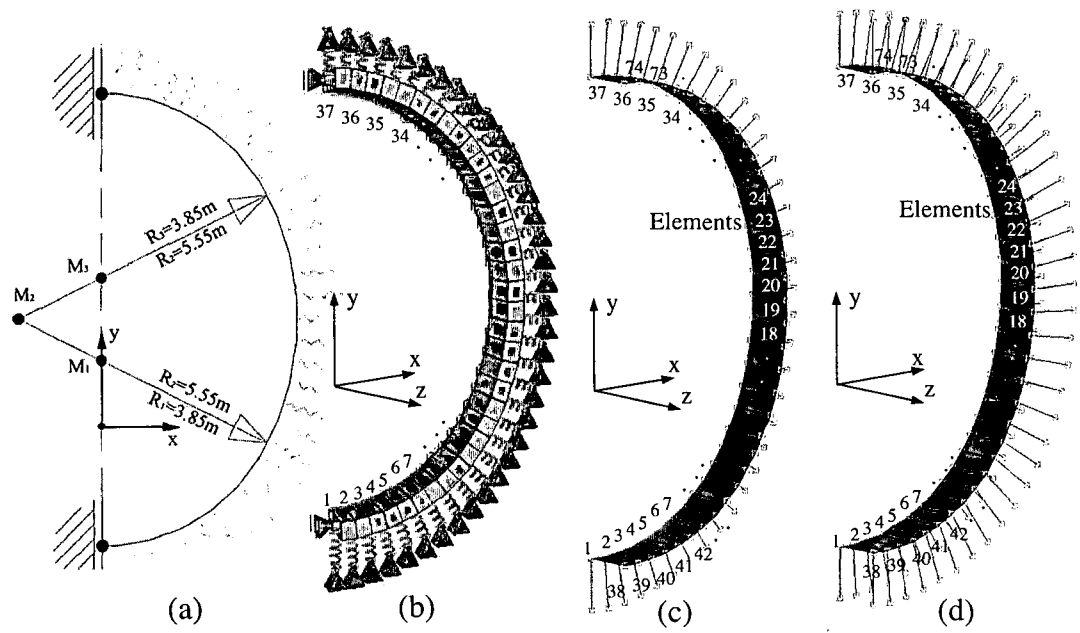

Figure 32: Tunnel cross-section: (a) geometric dimensions and FE models used in (b) SOFISTIK, (c) MARC-single row, and (d) MARC-double row

elements described by their central axis and the geometric properties b, h, and l [m]. The tunnel cross-section is discretized by means of 36 elements, giving 37 nodes and 37 spring elements representing the surrounding soil. In MARC, four node layered shell elements are used, giving $2 \times (36 + 1) = 74$ nodes (see Figure 32(c)). In a first step, a single row of springs is used (see Figure 32(c)). To connect the displacements of the second row of nodes to the nodes supported by the spring elements, a so-called tying option[4] is used. In

[4]The tying option is used in the MARC input-file to connect all degrees of freedom of the tied node to the degrees of freedom of the corresponding supported node (corresponding displacements u, v, and w and corresponding rotations ϕ_x, ϕ_y, and ϕ_z).

a second step, both rows of nodes are supported by spring elements (with an equivalent value for K) and the tying option was eliminated (see Figure 32(d)).

The following boundary conditions were considered:

- SOFISTIK: Springs are applied in the radial direction of the tunnel, representing the surrounding soil. In the longitudinal direction of the tunnel, no restraints are applied.
- MARC01:
  Springs are placed on one side of the cross-section. The other side is linked to the supported side by the so-called tying option. In addition, also the rotations in X- and Y-direction are restrained for every node (see Figure 32(c)). Because of the tying option, the deformation in the longitudinal direction is restrained.
- MARC02:
  Similar boundary conditions are assigned as in model MARC01, except that the X- and Y-rotations are not restrained.
- MARC03:
  The springs representing the soil are applied on both side of the cross-section. The X- and Y-rotations are restrained.
- MARC04:
  Similar boundary conditions are assigned as in model MARC03, except that the X- and Y-rotations are not restrained.

In the following, results will be presented for the equivalent temperature distribution (LC T_m and LC ΔT). Lateron, all load cases will be considered.

Figures 33 and 34 show the evolution of N and M obtained from SOFISTIK and MARC, showing no differences.

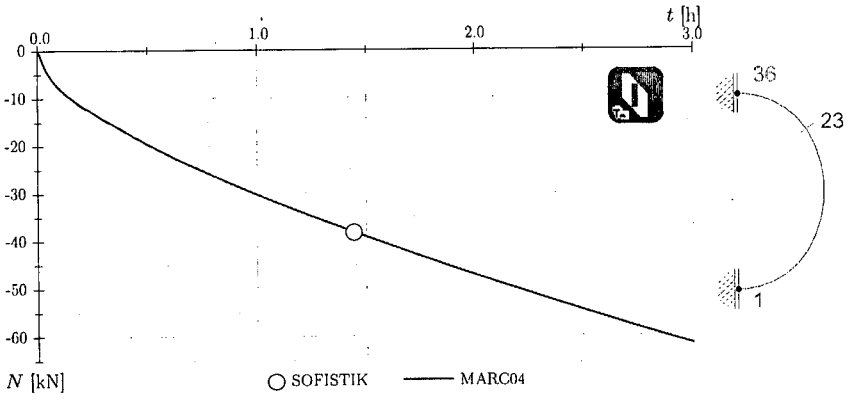

Figure 33: Results SOFISTIK and MARC04 – evolution of normal force in finite element 23 (LC T_m)

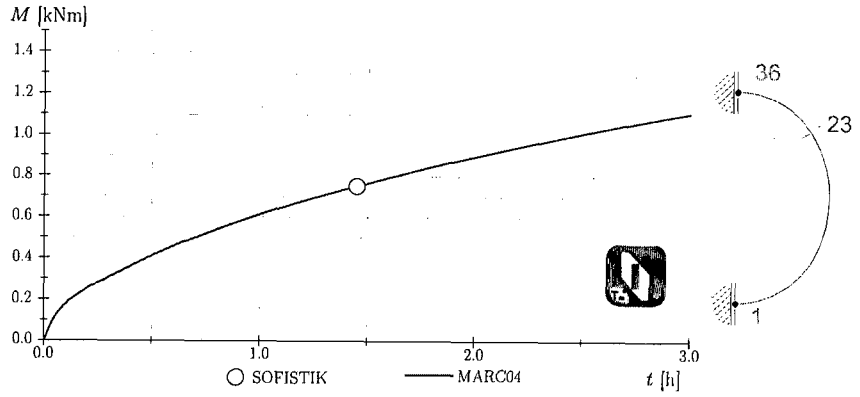

Figure 34: Results SOFISTIK and MARC04 – evolution of bending moment in finite element 23 (LC T_m)

In contrast to LC T_m, LC ΔT produces only bending moments. The respective evolution of M obtained from SOFISTIK and MARC04 is given in Figure 35. No differences between SOFISTIK and MARC04 is observed for LC ΔT.

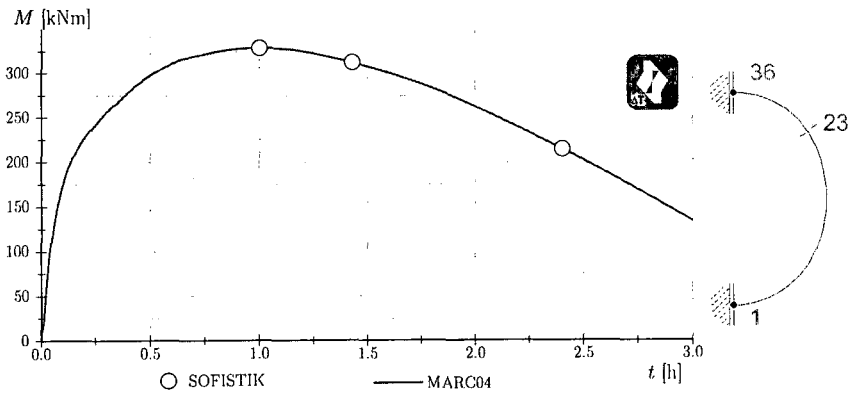

Figure 35: Results SOFISTIK and MARC04 – evolution of bending moment in finite element 23 (LC ΔT)

As indicated in Figure 36, showing the circumferential stress distribution in the inner layer, the boundary conditions considered for MARC04 assure a uniform stress distribution over the length of the tunnel. Accordingly, the bending moment is constant over the width of the tunnel.

Figure 37 shows the evolution of the bending moment for MARC01 calculation. First, the self-weight (LC G) is applied followed by a waiting period of 1 hour. Within the subsequent 10 hours, the earth load (LC E) is applied. After another waiting period of 8 hours, the equivalent temperature load (LC T_m and LC ΔT) is applied.

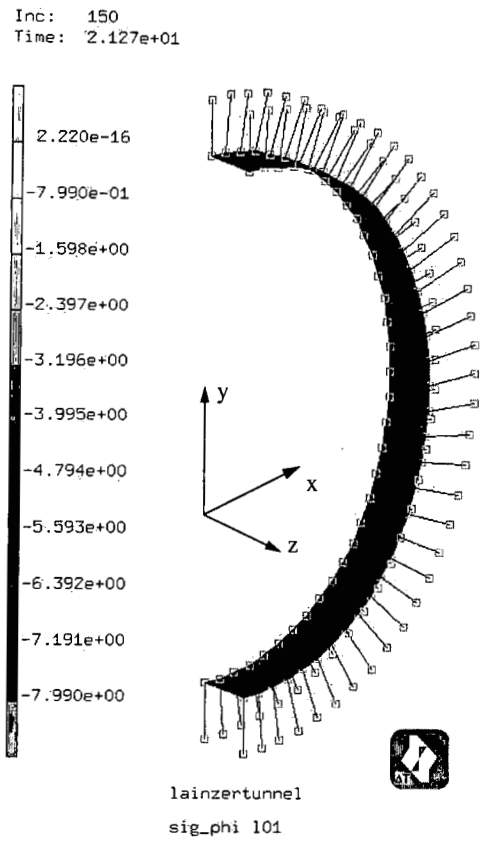

Figure 36: Results MARC04 – circumferential stress distribution σ_{phi} [MPa] in the inner layer at $t = 1.5$ h (LC ΔT)

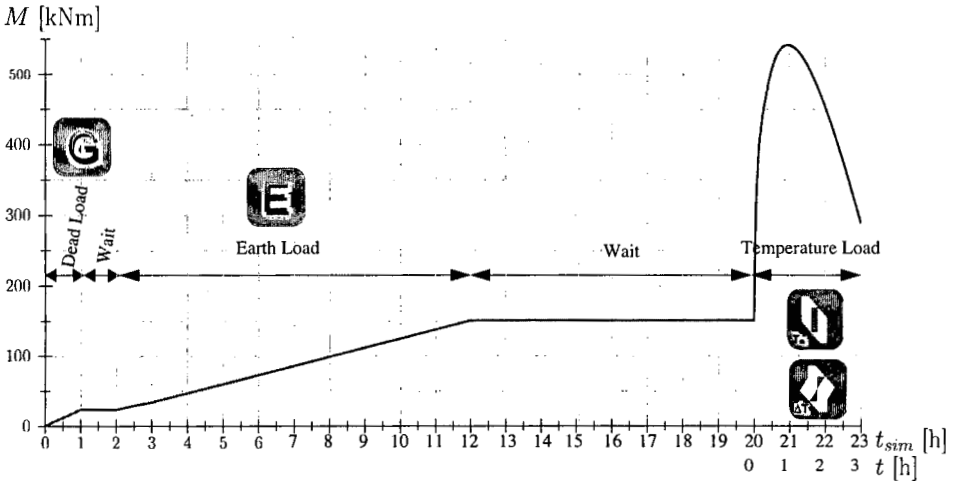

Figure 37: Results MARC01 – bending moment as a function of time in finite element 23 (All LC)

Figure 38 shows the circumferential stress in the first (inner) layer of the cross-section for MARC01 and all load cases are applied. In consequence of the tying option used in MARC01 the stresses are not uniform in Z-direction as shown in Figure 36.

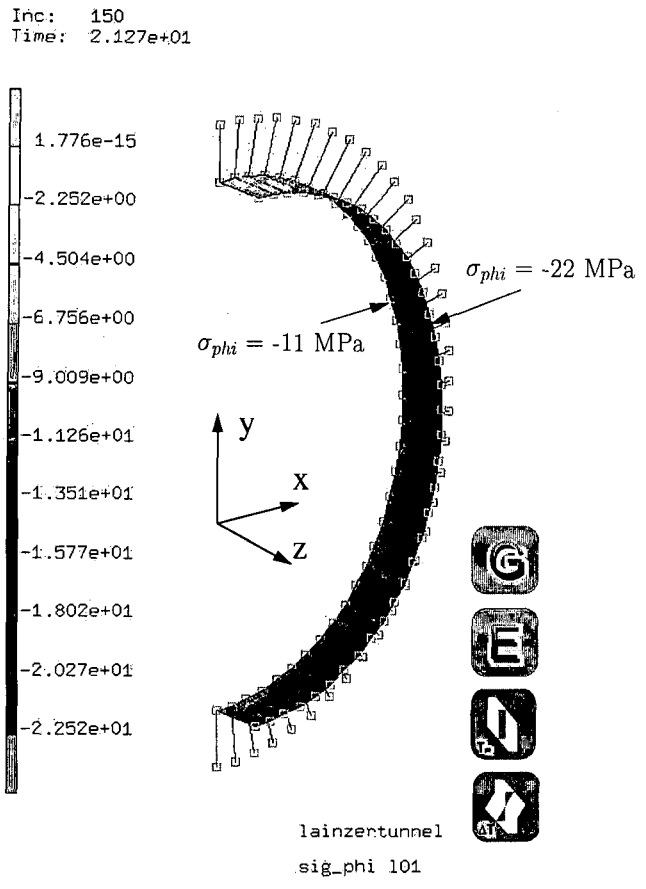

Figure 38: Results MARC – circumferential stress distribution σ_{phi} [MPa] in the inner layer at $t = 1.5$ h (All LC)

Figures 39 and 40 show the normal force and bending moment distribution obtained from SOFISTIK and MARC with all load cases applied (see also Tables 8 and 9 in Appendix A, providing numerical values). The magnitude of the normal force is continuously increasing from the top to the bottom of the tunnel.

The moment distribution shows equal results for MARC01 and MARC02. Moreover, restraining the X- and Y-rotations in MARC03 leads to a confinement in the longitudinal direction, giving similar results for the normal force and bending moment distribution as for MARC01 and MARC02. MARC04, characterized by no confinement in the longitudinal direction of the tunnel, gives a similar bending moment distribution as SOFISTIK.

Figure 41 shows the evolution of the bending moment with respect to time in finite element 23, showing a similar behavior as observed in Figure 40. Again, only small differences between MARC01, MARC02, and MARC03 are observed. MARC04 results agree best with the SOFISTIK results.

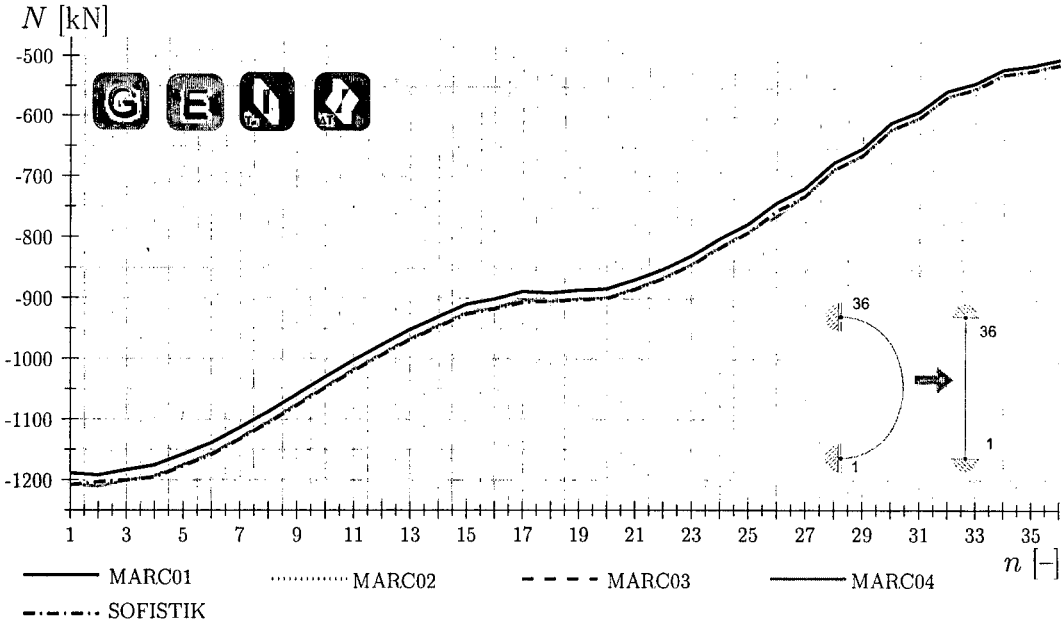

Figure 39: Results – normal force distribution for considered models at t = 1.43 h (All LC)

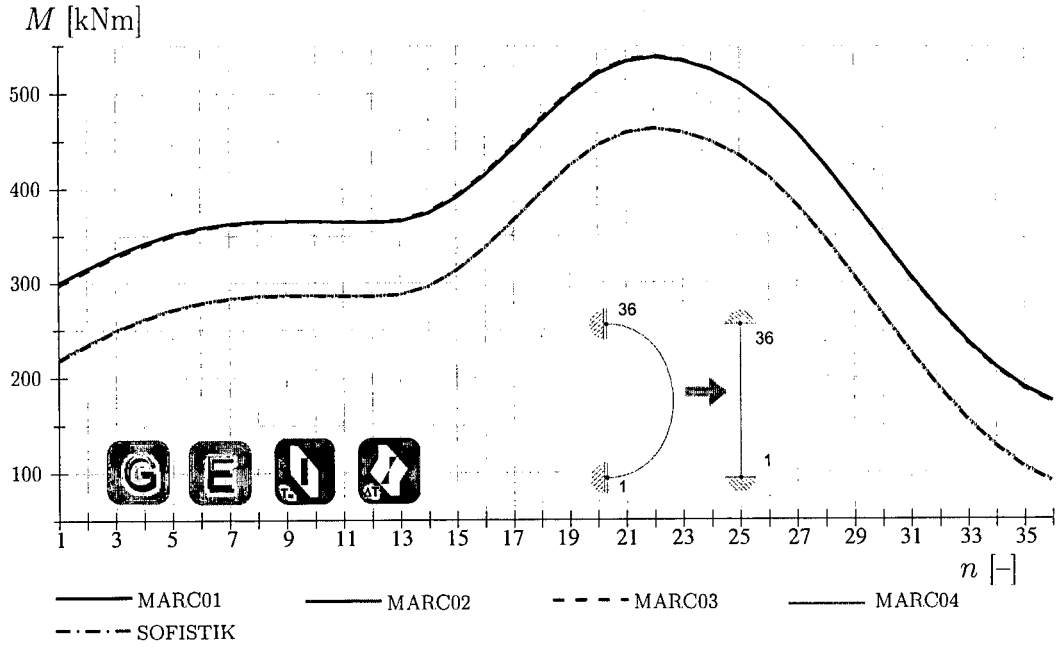

Figure 40: Results – bending moment distribution for considered models at t = 1.43 h (All LC)

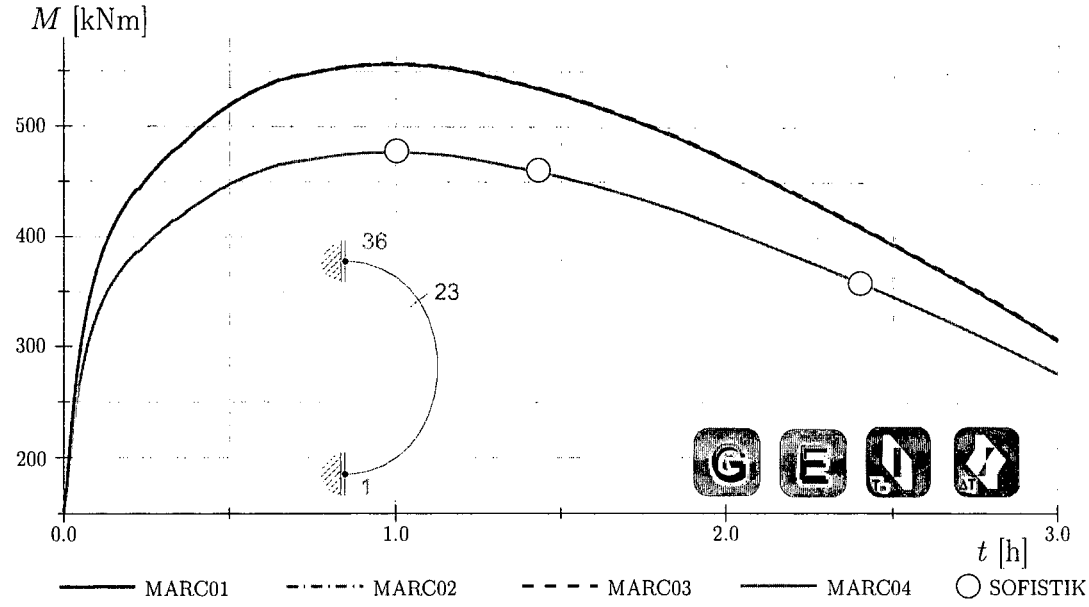

Figure 41: Results – bending moment as a function of time in finite element 23 (All LC)

The top displacement of the tunnel (Figure 42) can be used to assess the compliance of the tunnel support structure and to determine whether collapse of the structure occurs. Before application of the fire load, MARC01, MARC02, and MARC03 have exactly

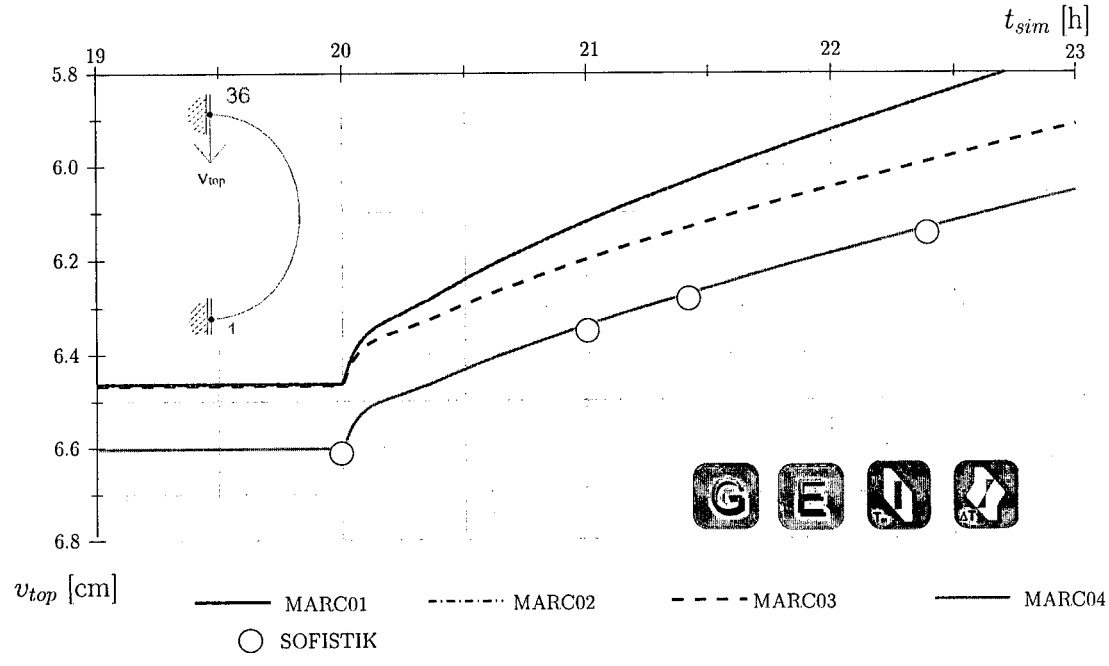

Figure 42: Results – top displacement as a function of time (All LC)

the same deformations. When fire loading is applied, MARC03, where the longitudinal displacement is not restrained, gives a larger top displacement. MARC04 and SOFISTIK have a similar top displacement history with, explained by no constraints in the longitudinal direction, giving higher magnitude compared to MARC01, MARC02, and MARC03.

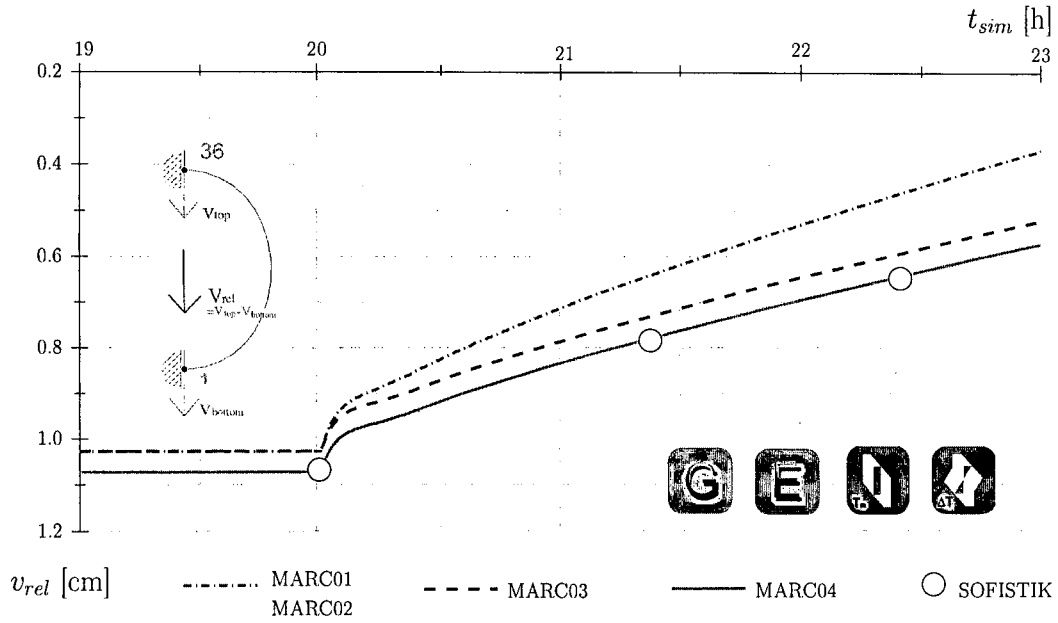

Figure 43: Results – relative displacement ($v_{top} - v_{bottom}$) as a function of time (All LC)

In order to investigate whether the overall shape of the tunnel expands or shrinks, the relative displacement $v_{rel} = v_{top} - v_{bottom}$ is determined (see Figure 43). According to Figure 43, the tunnel expands with temperature loading for all considered models. The top displacement v_{top} is decreasing (see Figure 42) while the bottom displacement v_{bottom} is influenced to a smaller extent. In general, the evolution presented in Figure 43 shows similarities to Figure 42. However, the results of the different models now show a smaller discrepancy than before. SOFISTIK and MARC04 produce the same relative displacements.

Remark: The slight variation between SOFISTIK and MARC04 is explained by the condition of plane cross-sections introduced by the shell formulation employed in MARC. Accordingly, an eigenstress state occurs in the longitudinal direction, leading to higher structural stiffness and slightly less displacements.

5 Results – linear-elastic / ideal-plastic material behavior

In the following simulations, the linear-elastic material model employed in the previous section is replaced by a linear-elastic / ideal-plastic material model (Figure 44(b)), where the compressive stresses are limited by the compressive strength f_c and the tensile stresses are limited by the tensile strength f_{ctm}.

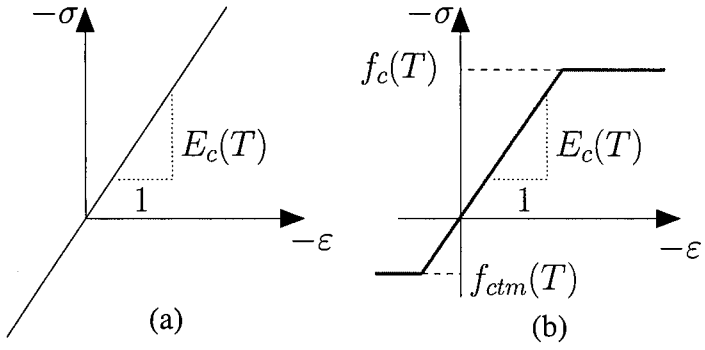

Figure 44: Stress-strain relationship for concrete: (a) linear-elastic and (b) linear-elastic / ideal-plastic material behavior

Within the analyses, material failure under compressive loading is modeled by a Drucker-Prager criterion, whereas the Rankine criterion is used to model cracking of concrete under tensile loading [Savov et al. (2005)].

5.1 Tunnel cross-section – equivalent temperature distribution (All LC)

Figure 45 illustrates the limitation of the tensile stresses by the tensile strength in case linear-elastic / ideal-plastic material behavior. In compression, the stresses reach about 25 MPa, hence the maximum compressive strength (f_c) is not reached. As a consequence the different stress distributions given in Figure 45, different normal forces and bending moments were obtained. As depicted in Figure 46, MARC04 (system with the least fixed boundary conditions), gives a higher normal force and a lower bending moment compared to MARC01 and MARC03. In addition, the normal force distribution presented in Figure 46 shows that the normal forces before temperature loading are different for linear-elastic and the linear-elastic / ideal-plastic material behavior. This is explained by the limitation of tensile stresses and, hence, the reduction of bending moments which is compensated by an increase of the normal force. Figure 47 shows the normal force in the longitudinal direction. Normal forces appear only in case of MARC01, where the displacement in the longitudinal direction is restrained. Between linear-elastic and linear-elastic / ideal-plastic material behavior, only a small difference is observed.

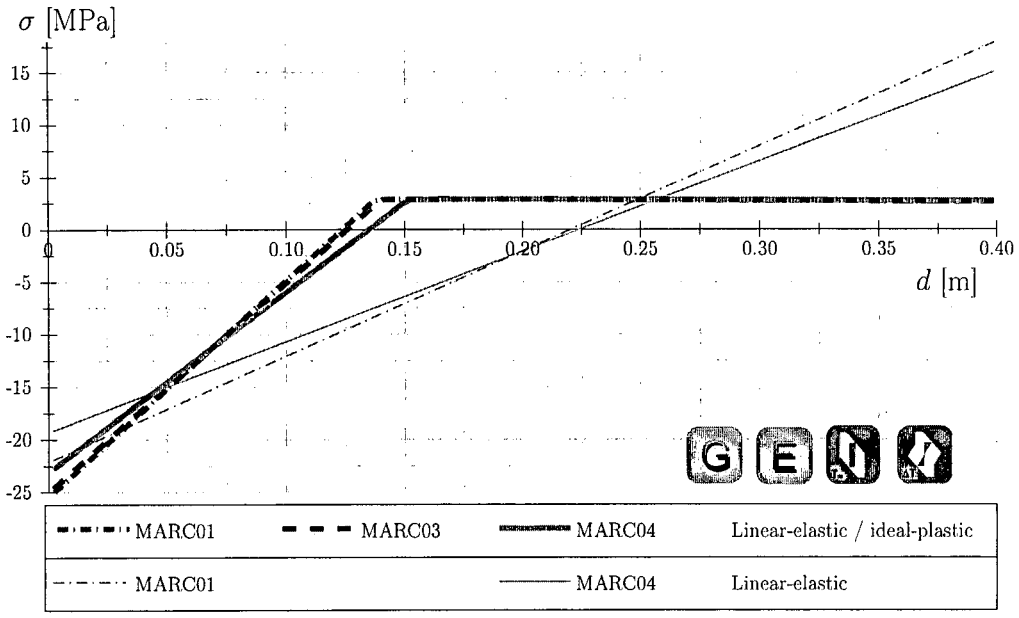

Figure 45: Results MARC – circumferential stress over lining thickness at $t = 1.43$ h in finite element 23 (All LC)

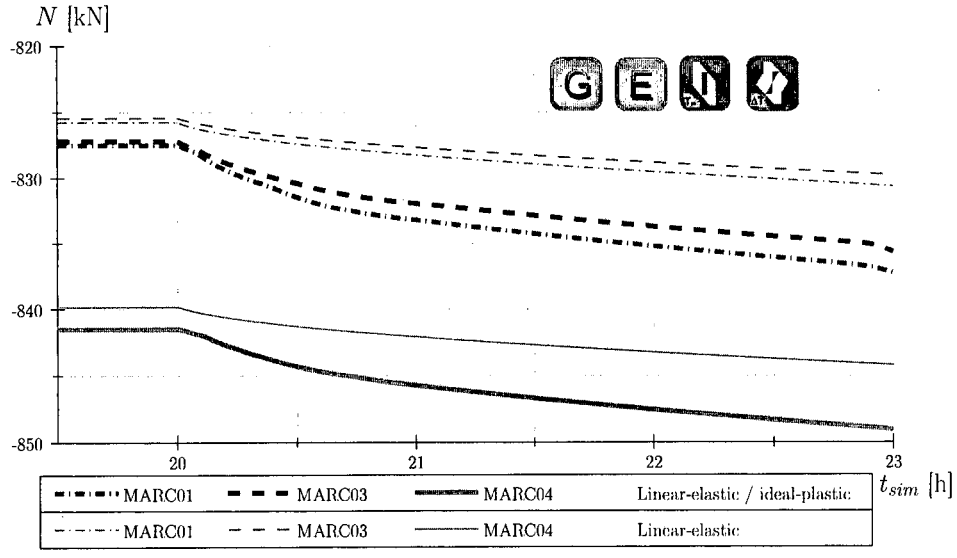

Figure 46: Results MARC – circumferential normal force as a function of time in finite element 23 (All LC)

Figure 48 shows the evolution of the bending moment for finite element 23. The differences between linear-elastic and linear-elastic / ideal-plastic calculation are significant. The maximum value at finite element 23 decreases from 550 kNm and 470 kNm to 320 kNm and 310 kNm, respectively. For the case of linear-elastic / ideal-plastic material behavior, the differences between MARC01, MARC03, and MARC04 are marginal. The

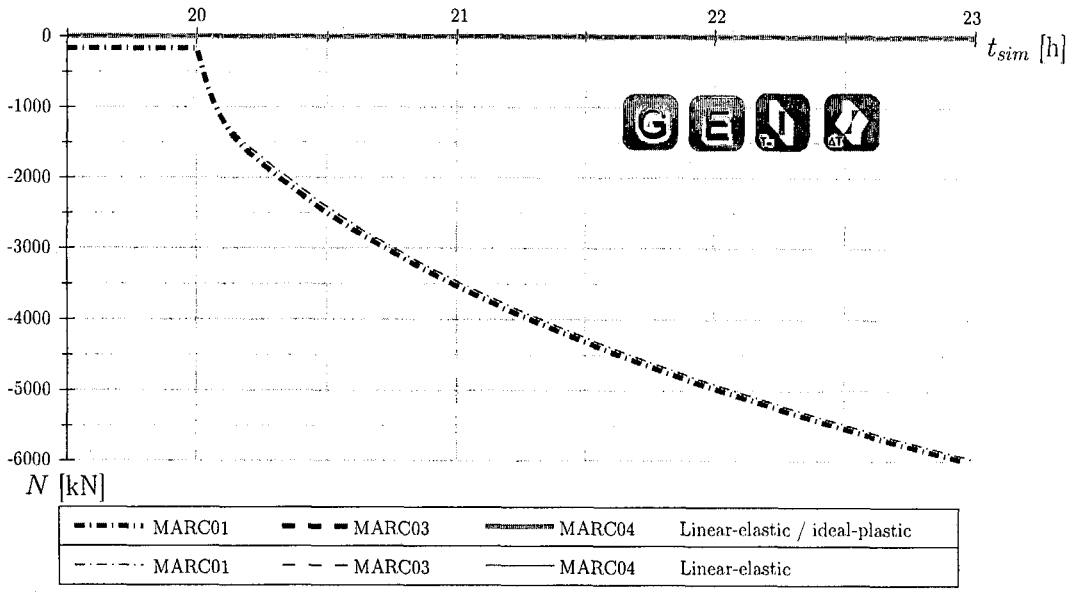

Figure 47: Results MARC – longitudinal normal force as a function of time in finite element 23 (All LC)

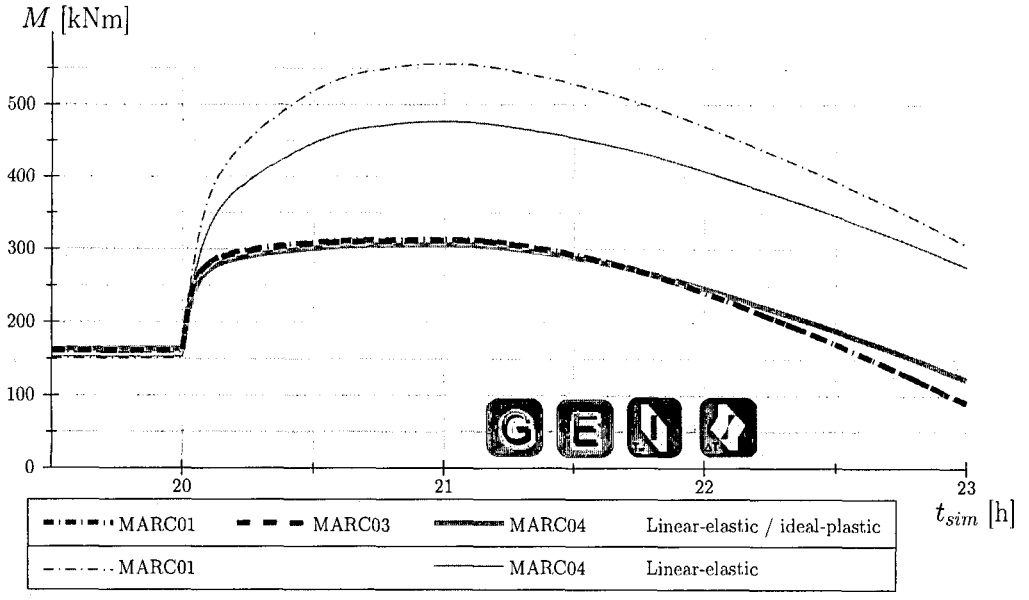

Figure 48: Results MARC – circumferential bending moment as a function of time in finite element 23 (All LC)

longitudinal bending moment as a function of time is presented in Figure 49. While MARC01 and MARC03 show the same evolution of the bending moment when considering linear-elastic material behavior, differences in the evolution of the bending moment occur in case of linear-elastic / ideal-plastic material behavior. This differences (i.e., the moment is more reduced in case of MARC03 compared to MARC01) are explained by the

boundary conditions employed in MARC03, constraining only the rotations in the X- and Y-direction. The missing (compressive) normal force in the longitudinal direction favors cracking in the tensile-loaded regime, reducing the bending moment for MARC03.

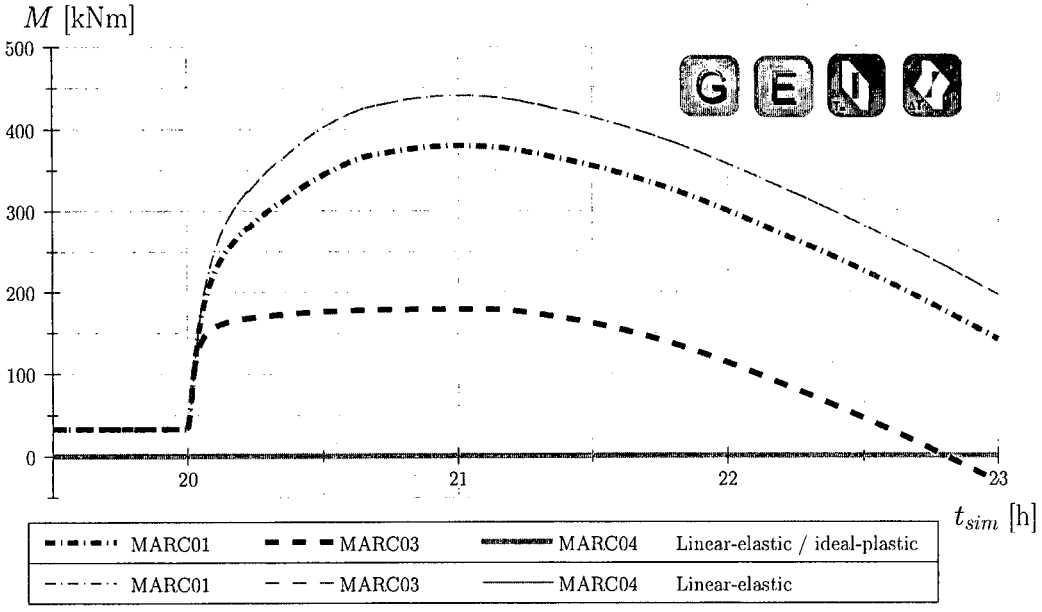

Figure 49: Results MARC – longitudinal bending moment as a function of time in finite element 23 (All LC)

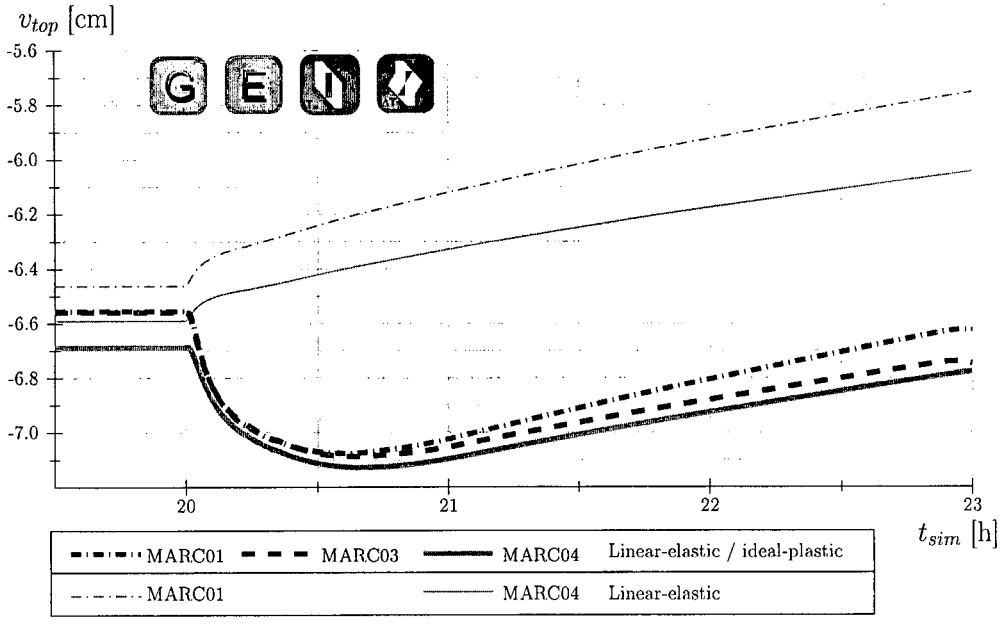

Figure 50: Results MARC – top displacement as a function of time (All LC)

Finally, the top displacement given in Figure 50 illustrates the influence of the employed material models on the deformation of the tunnel lining. The considered linear-elastic / ideal-plastic material behavior increases the compliance of the tunnel support structure compared to linear-elastic material behavior. Accordingly, right at the beginning of temperature loading, the displacement increases by approximately 0.5 cm which is explained by cracking of concrete when fire loading starts.

5.2 Tunnel cross-section – nonlinear temperature distribution (All LC)

The circumferential stress distribution obtained from application of the nonlinear temperature distribution is presented in Figure 51. In addition, also the longitudinal stress is given. The stresses in compression reach the biaxial compressive strength. At the boundary of the tensile-loaded regime (close to the outer surface of the tunnel lining), compressive stresses are observed. These stresses result from the restriction to plane cross-sections, causing longitudinal stress and, via Poisson's effect, influencing the stress component in the circumferential direction.

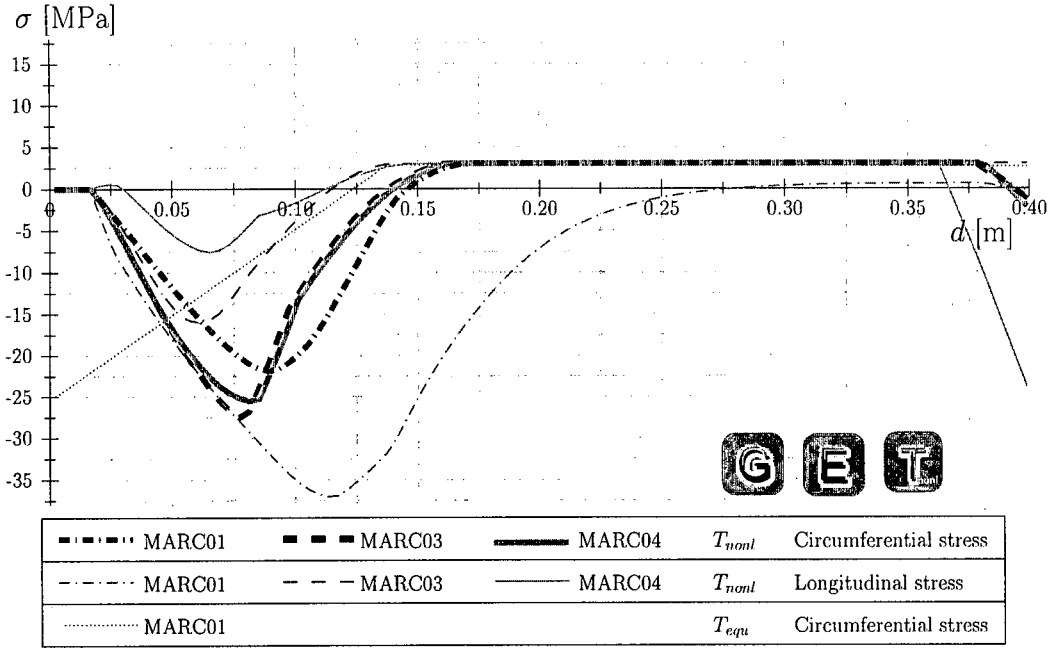

Figure 51: Results MARC – stress distributions over lining thickness at t = 1.43 h in finite element 23 (All LC)

In comparison to the results obtained by using the equivalent temperature, also the stresses close to the heated surface are different when using T_{nonl} (see Figure 51). Within the first 2 cm of the lining, the stresses are equal to zero which is explained by the temperature exceeding 800°C. This results in a decrease of Young's modulus and the strength of concrete (see Figure 4) to zero, giving no stresses in this region of the lining.
As regards longitudinal stress, the stress obtained from MARC01 is much larger than for MARC03 or MARC04, which is explained by the tying option, restraining the longitudinal dilatation. In case of MARC01 and MARC03, the X- and Y-rotations of the nodes are restrained, resulting in a non-zero normal force only in case of MARC01 and a bending moment in longitudinal direction in both cases. Due to the fact that the dilatation in longitudinal direction is not fixed in case of MARC03, the stresses are smaller than for MARC01 and no normal forces occur. MARC04 produces the smallest stresses in longi-

tudinal direction since the boundary conditions do not hinder longitudinal dilatation nor rotation in X- and Y-direction. Hence, the stress resultants in the longitudinal direction are zero even though the restriction to plane cross-sections causes development of stresses in the longitudinal direction.

The previously presented results (for T_{equ}) show very small differences in the normal force between the different models. As shown in Figure 52, the nonlinear temperature load results in a significant increase of the normal force in comparison to the results under consideration of the equivalent temperature load. This difference is explained by structural effects resulting in force re-arrangement.

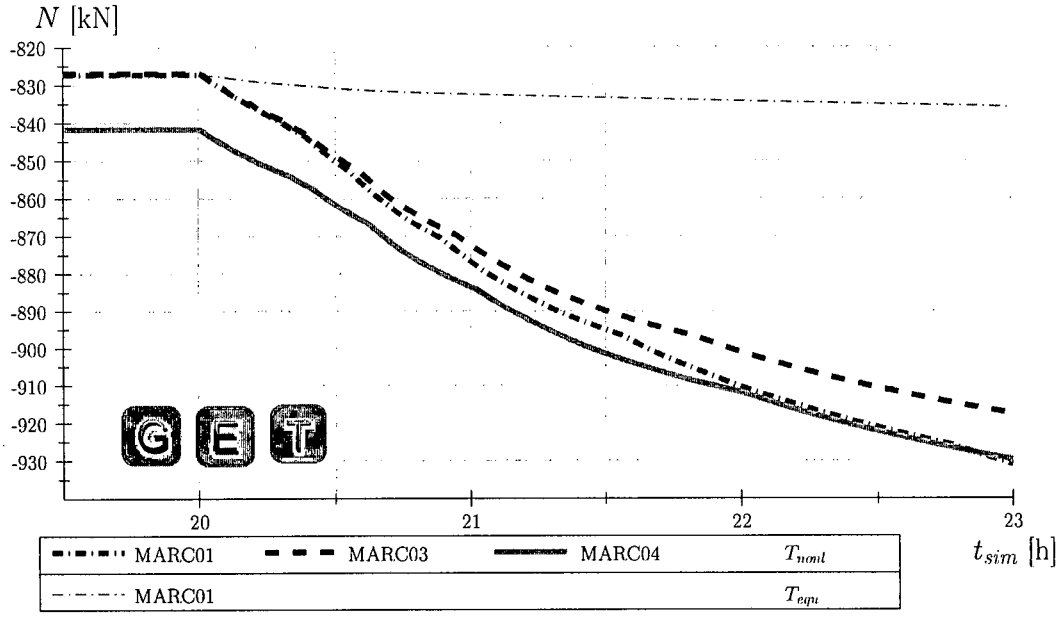

Figure 52: Results MARC – normal force as a function of time in finite element 23 (All LC)

In Figure 53, the normal force distribution over the tunnel cross-section at $t = 1.43$ h is presented for the MARC04 model. The normal force is increasing from the top to the bottom of the tunnel cross-section, with higher normal forces in case the nonlinear temperature distribution is applied. This is explained by force re-arrangement in consequence of plastic deformations, leading to higher deformations and the observed increase in the normal force.

The evolution of the bending moment in finite element 23 is given in Figure 54, showing a different development when considering T_{nonl}. The differences between the models are mainly caused by the deformation constraints in the longitudinal direction with the difference increasing with continuation of fire loading. In case of MARC04, enforcing only plane cross-sections, the largest value for the bending moment is obtained.

Figure 55 shows the distribution of the bending moment over the tunnel cross-section. Hereby, the bending moments are significantly decreased by consideration of linear-elastic / ideal-plastic material behavior. The maximum value of the bending moment (finite

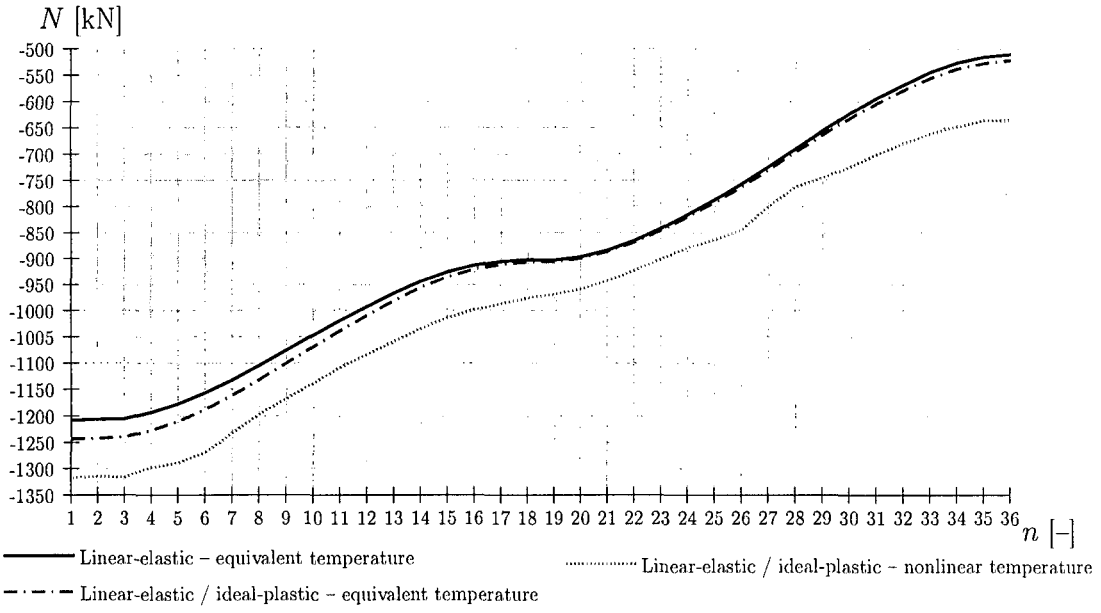

Figure 53: Results MARC04 – normal force distribution over tunnel cross-section at $t = 1.43$ h (All LC)

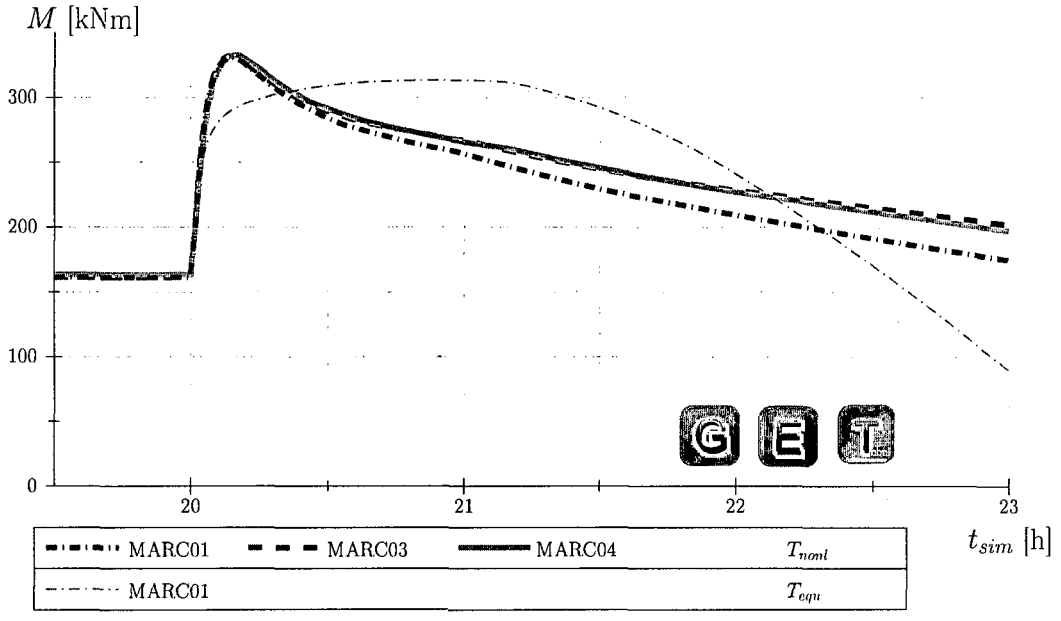

Figure 54: Results MARC – bending moment as a function of time in finite element 23 (All LC)

element 23) is reduced by 40%. Considering the nonlinear temperature distribution, the distribution of the bending moment becomes more uniform in consequence of force re-arrangement caused by plastic deformations.

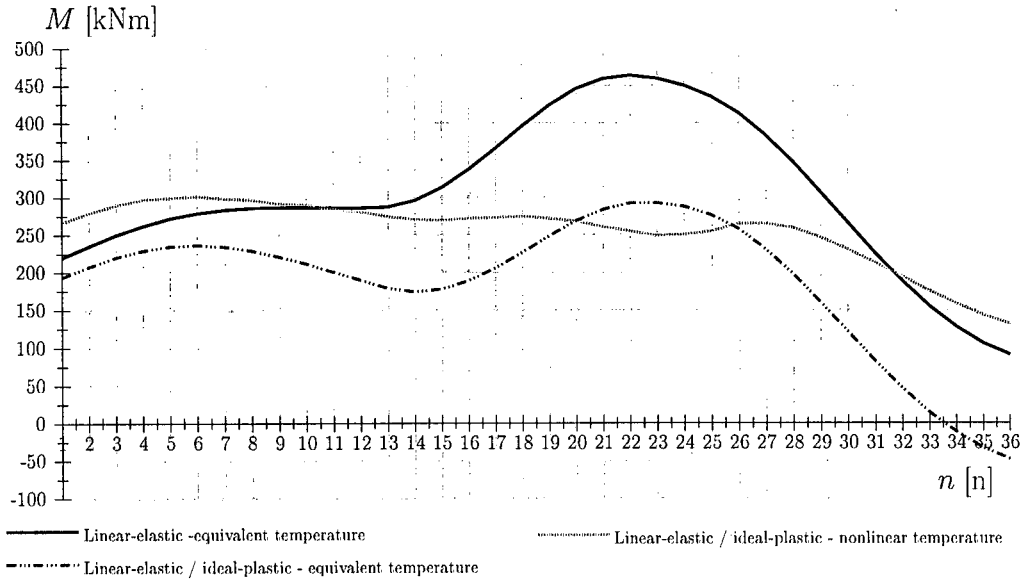

Figure 55: Results MARC04 – bending moment distribution over tunnel cross-section at $t = 1.43$ h (All LC)

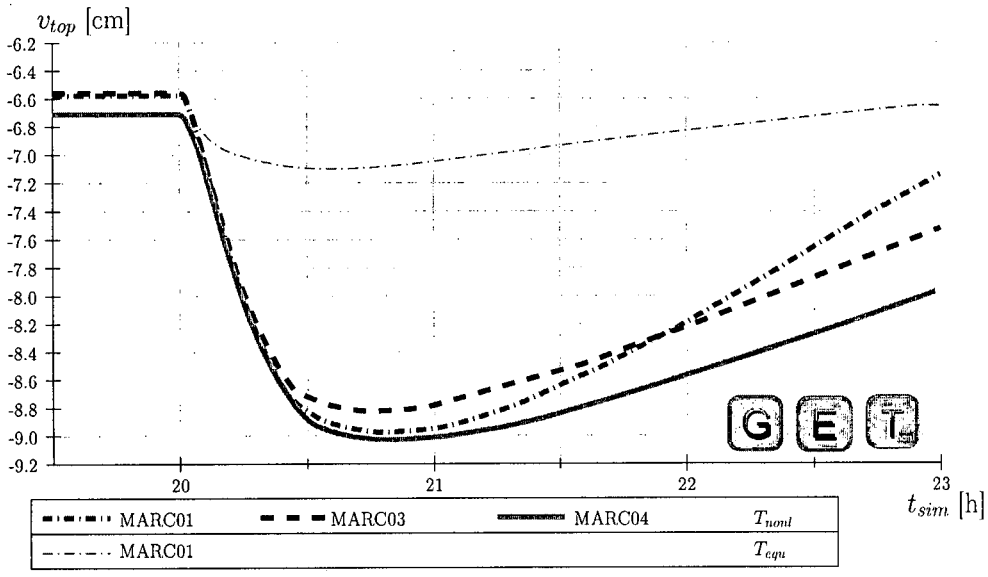

Figure 56: Results MARC – top displacement as a function of time (All LC)

Figure 56 illustrates the increase of displacements in case of the nonlinear temperature loading is considered, which is explained by plastic deformations occurring in the compression zone during fire loading, increasing the compliance of the tunnel-support structure. Moreover, differences between the models are observed. Towards the end of fire loading, the compensation of the vertical displacement by thermal dilation is the highest for MARC01, which is explained by the deformation constraints in the longitudinal direction.

6 Concluding remarks and outlook

The performed analyses of concrete structures under fire load showed that the assumption of linear-elastic material behavior leads to an overestimation of the internal stress resultants. When compared with the analysis results based on a linear-elastic / ideal-plastic material behavior this overestimation reached values of up to approximately 85% for the considered tunnel cross-section.

The analyses performed with the FE program SOFISTIK were characterized by linear-elastic material behavior and equivalent temperature distributions were employed. Hence, no redistribution of internal forces in consequence of cracking was considered, resulting in an underestimation of the structural compliance. The FE program MARC, on the other hand, allows calculations with increased complexity (linear-elastic / ideal-plastic material behavior, nonlinear temperature, etc.), giving more realistic results.

The main objective of this work was to investigate the applicability of the equivalent temperature concept. The equivalent temperature distribution was obtained from a clamped-beam system. The application of this concept to tunnel structures showed significant differences in loading and deformation of the structure. Therefore, application of the nonlinear temperature distribution (instead of the equivalent temperature distribution) should be favored, giving more realistic results.

Based on the obtained results, the need for direct consideration of nonlinear temperature distributions in the structural analyses is demonstrated. Future work will focus on the implementation of the necessary tools (layered shell elements, elasto-plastic material behavior) into commercial structural design programs (such as, e.g., SOFISTIK), in order to enable realistic analyses of fire loading of concrete structures.

References

Ahmed, K. A. M. (2004). *Numerical modelling of tunnel lining at high temperature using sandwich element.* PhD thesis, University of Innsbruck, Innsbruck, Austria.

El-Arabi, I. A., Duddeck, H., and Ahrens, H. (1992). Structural analysis for tunnels exposed to fire temperatures. *Tunneling and Underground Space Technology*, 7(1):19–24.

Horvath, J. (2003). *Beiträge zum Brandverhalten von Hochleistungsbeton [Contributions to the behavior of high-performance concrete under fire].* PhD thesis, Vienna University of Technology, Vienna, Austria. In German.

Kusterle, W. and Lindlbauer, W. (2004). Zur Brandbeständigkeit von Beton: Rückschlüsse aus Ergebnissen an Großversuchskörpern [Fire resistance of concrete: conclusions from large-scale tests]. *Schriftenreihe der Österreichischen Vereinigung für Beton- und Bautechnik.* In German.

Kusterle, W., Lindlbauer, W., Hampejs, G., Heel, A., Donauer, P.-F., Zeiml, M., Brunnsteiner, W., Dietze, R., Hermann, W., Viechtbauer, H., Schreiner, M., Vierthaler, R., Stadlober, H., Winter, H., Lemmerer, J., and Kammeringer, E. (2004). Brandbeständigkeit von Faser-, Stahl- und Spannbeton [Fire resistance of fiber-reinforced, reinforced, and prestressed concrete]. Technical Report 544, Bundesministerium für Verkehr, Innovation und Technologie, Vienna. In German.

Pichler, C., Lackner, R., and Mang, H. A. (2006). Safety assessment of concrete tunnel linings under fire load. 132(6):961–969.

prEN1992–1–2 (2004). *Eurocode 2 - Bemessung und Konstruktion von Stahlbeton- und Spannbetontragwerken - Teil 1-2: Allgemeine Regeln - Tragwerksbemessung für den Brandfall [Eurocode 2 - Design of concrete structures - Part 1-2: General rules - Structural fire design].* European Committee for Standardization (CEN). In German.

Richter, E. and Hosser, D. (2002). Baulicher Brandschutz bei Verkehrstunneln in offener Bauweise [fire protection for tunnels]. *Beton- und Stahlbetonbau*, 97(4):178–184. In German.

Savov, K., Lackner, R., and Mang, H. A. (2003). Stability assessment of shallow tunnels subjected to fire load. In Oñate, E. and Owen, D., editors, *CD-ROM Proceedings of the 7th International Conference on Computational Plasticity (COMPLAS 2003)*, Barcelona. CIMNE. 17 pages.

Savov, K., Lackner, R., and Mang, H. A. (2005). Stability assessment of shallow tunnels subjected to fire load. *Fire Safety Journal*, 40:745–763.

Schrefler, B. A., Brunello, P., Gawin, D., Majorana, C. E., and Pesavento, F. (2002). Concrete at high temperature with application to tunnel fire. *Comput Mech*, 29:43–51.

Wageneder, J. (2002). Traglastuntersuchungen unter Brandeinwirkungen [Ultimate load investigations considering fire load]. *Bauingenieur*, 77:184–192. In German.

Zeiml, M. (2004). Analytical and numerical modeling of heat and water-vapor transport in concrete subjected to fire loading. Master's thesis, Vienna University of Technology, Vienna, Austria.

Zeiml, M., Lackner, R., Pesavento, F., and Schrefler, B. A. (2008). Thermo-hydro-chemical couplings considered in safety assessment of shallow tunnels subjected to fire load. *Fire Safety Journal*, 43(2):83–95.

A Tables

Element	SOFISTIK	MARC01	MARC02	MARC03	MARC04
[Nr.]	N [kN]	N [kN]	N [kN]	N [kN]	N [kN]
1	-1208.3	-1189.2	-1189.2	-1188.0	-1207.4
2	-1203.6	-1192.5	-1192.5	-1191.1	-1210.8
3	-1200.7	-1183.6	-1183.6	-1181.5	-1201.7
4	-1196.1	-1176.0	-1176.0	-1174.1	-1194.1
5	-1177.8	-1158.0	-1158.0	-1156.3	-1175.8
6	-1159.1	-1139.5	-1139.5	-1138.1	-1157.1
7	-1133.4	-1114.3	-1114.3	-1113.1	-1131.6
8	-1106.7	-1087.9	-1087.9	-1087.2	-1104.8
9	-1077.5	-1059.2	-1059.2	-1058.7	-1075.6
10	-1048.3	-1030.3	-1030.3	-1030.3	-1046.5
11	-1020.2	-1002.6	-1002.6	-1002.8	-1018.4
12	-994.0	-976.8	-976.8	-977.3	-992.2
13	-968.3	-951.5	-951.5	-952.1	-966.6
14	-946.9	-930.4	-930.4	-931.2	-945.3
15	-925.8	-909.6	-909.6	-910.4	-924.2
16	-917.2	-901.1	-901.1	-901.8	-915.6
17	-906.3	-888.3	-888.3	-888.8	-902.7
18	-904.2	-890.4	-890.4	-890.4	-904.9
19	-901.8	-886.0	-886.0	-885.6	-900.5
20	-899.7	-883.7	-883.7	-883.0	-898.4
21	-884.4	-868.7	-868.7	-868.0	-883.3
22	-866.6	-851.1	-851.1	-850.4	-865.5
23	-843.7	-828.7	-828.7	-828.1	-842.8
24	-815.2	-800.6	-800.6	-800.2	-814.4
25	-790.2	-776.1	-776.1	-775.4	-789.3
26	-754.6	-741.1	-741.1	-740.5	-763.3
27	-729.5	-716.5	-716.5	-716.1	-729.0
28	-685.9	-673.7	-673.7	-673.4	-685.5
29	-662.1	-650.3	-650.3	-650.2	-661.6
30	-618.8	-607.8	-607.8	-607.8	-618.6
31	-599.3	-588.6	-588.6	-588.8	-599.2
32	-563.5	-553.5	-553.5	-553.7	-563.7
33	-550.2	-540.5	-540.5	-539.6	-548.4
34	-526.2	-517.0	-517.0	-517.4	-523.8
35	-519.8	-510.7	-510.7	-511.2	-517.8
36	-508.9	-500.0	-500.0	-499.1	-506.9

Table 8: Numerical results – normal force for different models at $t = 1.43$ h (All LC)

Element	SOFISTIK	MARC01	MARC02	MARC03	MARC04
[Nr.]	M [kNm]	M [kNm]	M [kNm]	M [kNm]	M [kNm]
1	218.0	300.0	300.0	297.6	219.6
2	233.3	314.9	314.9	312.6	234.6
3	248.4	329.6	329.6	327.3	249.5
4	260.6	341.4	341.4	339.3	261.6
5	270.7	351.3	351.3	349.4	271.8
6	277.8	358.1	358.1	356.5	278.7
7	282.5	362.4	362.4	361.2	283.3
8	285.0	364.8	364.8	363.9	285.7
9	285.7	365.2	365.2	364.7	286.4
10	286.0	365.3	365.3	365.2	286.6
11	285.3	364.4	364.4	364.8	285.9
12	285.3	364.1	364.1	364.9	285.7
13	287.0	365.5	365.5	366.7	287.2
14	295.8	373.9	373.9	375.6	295.8
15	313.1	390.6	390.6	392.6	312.8
16	337.0	413.9	413.9	416.2	336.5
17	365.6	441.8	441.8	444.3	364.9
18	395.7	471.3	471.3	473.8	394.9
19	423.8	498.8	498.8	501.2	423.0
20	445.9	520.7	520.7	522.8	445.3
21	459.1	533.7	533.7	535.4	458.6
22	463.5	538.3	538.3	539.5	463.2
23	459.3	534.3	534.3	535.2	459.3
24	449.8	525.2	525.2	525.7	449.9
25	434.7	510.6	510.6	510.8	435.1
26	412.8	489.3	489.3	489.1	413.4
27	382.3	459.5	459.5	459.1	383.2
28	346.1	424.2	424.2	423.5	347.2
29	305.8	384.8	384.8	383.9	307.0
30	264.8	344.8	344.8	343.6	266.1
31	224.1	305.1	305.1	303.8	225.6
32	186.9	268.9	268.9	267.4	188.4
33	153.5	236.3	236.3	234.8	155.1
34	126.2	209.8	209.8	208.2	127.8
35	104.3	188.6	188.6	186.9	105.8
36	89.2	174.0	174.0	172.3	90.6

Table 9: Numerical results – bending moment for different models at $t = 1.43$ h (All LC)

B Determination of equivalent temperature distribution

The equivalent temperature distribution is determined considering, a clamped beam (see Figure 15), aiming at equal normal forces and bending moments for (i) the nonlinear temperature distribution and linear-elastic / ideal-plastic material behavior and (ii) the equivalent temperature distribution and linear-elastic material behavior.

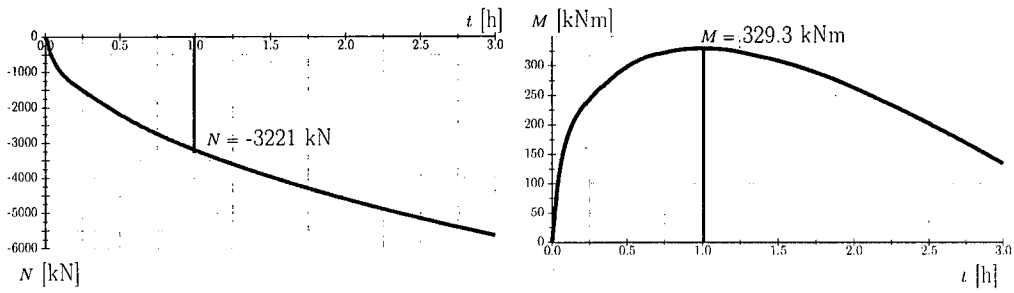

Figure 57: Results MARC – normal force and bending moment as a function of time assuming linear-elastic / ideal-plastic material behavior (LC T_{nonl})

In a first step, the evolution of the normal force and the bending moment is calculated considering the nonlinear temperature distribution assuming linear-elastic / ideal-plastic material behavior (see Figure 57).

Based on the obtained normal force and bending moment, T_m and ΔT are computed according to Equations (5) and (6) (see Subsection 3.2).

Figure 58: Results SOFISTIK – normal force and bending moment at $t = 1.00$ h (LCs T_m and ΔT)

T_m and ΔT serve as input for SOFISTIK, assuming linear-elastic material behavior (see Figure 58 for normal force and bending moment at $t = 1.00$ h). The obtained results prove the applicability of the equivalent temperature concept for the special case of a clamped beam. The observed discrepancy between the normal force and bending moment obtained from SOFISTIK and MARC is explained by the restriction to plane cross-sections in MARC, inducing stress states perpendicular to the beam axes. These biaxial stress states may exceed the uniaxial strength, as the biaxial strength f_b was set equal to 1.16 f_c.